Design of a locomotive system for the exploration of rugged and deformable terrain

Gaetan Pans

TU Delft

Design of a locomotive system for the exploration of rugged and deformable terrain

By

Gaetan Pans

Master Thesis (ME54035)

in partial fulfilment of the requirements for the degree of

Master of Science
in Mechanical Engineering

at the Department Maritime and Transport Technology of the Faculty Mechanical, Maritime and Materials Engineering of Delft University of Technology
To be defended publicly on August 31, 2024 at 10:00am

Student Number:	5858372
MSc track:	Multi-Machine Engineering
Report number:	2024.MME.8989
Thesis Supervisor:	Dr. J.Jovanova
Thesis Chair:	Dr. J.Jovanova
Committee Member:	Dr. A. Napoleone
Date:	September 30, 2024

Acknowledgements

I would like to express my appreciation and gratitude towards Dr. Jovana Jovanova for making this project possible. The constant support and stimulating academic discussions have greatly contributed to the depth and quality of the work presented in this thesis. Furthermore, I would also like to acknowledge with much appreciation my peers specifically Siddharth Sasidharan for countless hours of back-and-forth problem-solving and brainstorming when an external opinion was needed. Finally, I would like to thank my family for the constant support given throughout my entire academic journey.

Abstract

The importance of natural environments with rugged deformable terrain (marshes, mangroves, rainforests, coastlines) from biodiversity, carbon capture, and coastal protection to economic livelihood is significant. However, the current systems available for robots to explore those ecosystems are either large, expensive and intrusive, not application focused or consist of custom components that are difficult to integrate with existing robotic mechanisms. This thesis proposes a novel soft adaptable wheel suited for such ecosystems. The mechanism operates as a soft fluidic actuator constructed with Dragon Skin 30 able to change its form depending on the task at hand. Various designs were simulated in MuJoCo to test its ability to overcome rigid obstacles and terrain forms (from ramps, steps, smooth undulating terrain and terraced undulating terrain). The design's structural feasibility was then tested and further improved using Ansys with the final result having a loading capacity of 1.25N (at 0kPa) and a maximum blocked force of 1.98N (at 35kPa). Finally, the wheel was tested at 3 distinct operating configurations (neutral, partial and fully inflated) in 4 types of deformable terrain (non-compressible dry, compressible dry, non-compressible sticky, compressible sticky) using EDEM Altair. This evaluated its performance and validated the need for different forms according to the rheological properties of the terrain. The design proposed in this paper is intended to be more application-focused, with its simplicity facilitating integration into robotic systems, using off-the-shelf components, and ultimately reducing the time required to be used in environmental applications.

Keywords
Soft Robotics, Deformable Terrain, Soft Fluidic Actuator, Adaptable, Locomotion

Contents

Nomenclature

ϵ	Strain
Γ	Potential Energy
λ_i	Stretch Ratios
Ψ	Strain Energy Function
θ	Bending angle
C_1, C_2, C_3	Material Constants
D	Flexural rigidity
E	Elastic modulus
h	Total height of a chamber
h_1	Distance from the base of a chamber to the top of the strain-limiting layer
h_c	Distance to the center line of the ellipse
I	Moment of inertia of the chamber
i	Subscript i refers to the property when inflated
I_1, I_2, I_3	Principal Invariants
k	Curvature
L_i	Undeformed Length
l_i	Deformed Length
N	Number of chambers
P_i	Inflation pressure
R	Radius of curvature
U	Internal Strain Energy
V_i	Inflated volume of a chamber
W_p	Work Potential
x	Original chamber width
x_i	Maximum inflated chamber width at the center of the ellipse
DEM	Discrete Element Method
FEA	Finite Element Analysis
LC	Loading Configurations
SFA	Soft Fluidic Actuators

List of Figures

List of Tables

1| Introduction

Despite the abundance of natural environments made up of rugged deformable terrain (e.g sand, soil, forests, marshes, mud, loose leaves), robotic systems that can locomote over such terrain without damaging it are scarce. The current commercial systems (e.g. offroad vehicles) are usually large, damaging and expensive, limiting our ability to explore those areas. Economically, 40% of the world's population lives in coastal regions [32]. Furthermore, coastal "blue carbon" ecosystems (tidal marshes, mangrove forests, seagrass meadows) can store 30 to 50 times more carbon than traditional terrestrial forests [18]. Hence, the ability to explore and traverse these areas with low-cost efficient robotic systems can prove to be extremely beneficial. Such applications may include environmental surveillance to preserve biodiversity, maintenance and inspection of coastal structures, reforestation of forests, monitoring of soil erosion and more. This paper aims to outline the design goals for the project, review the current state of research in this field, before presenting the main body of work of designing the proposed solution.

1.1. Design Goals

For the design of the locomotive system, the following design goals were set as a benchmark. Through this, each iteration could be tested against a set of quantitative measures to make it suitable for the desired terrain. The design goals set for the project were as follows:

- Able to locomote over deformable terrain of varying moisture levels. Specifically, the following classifications (more details in chapter 6):
  - Non-compressible dry
  - Compressible dry
  - Non-compressible sticky
  - Compressible sticky
- Able to overcome varying obstacles, steps and inclines as follows (more details in chapter 3):
  - Maximum Step Height: 0.2m
  - Maximum Degree Incline: 17.5°
  - Undulating Terrain Ranging: 0 - 1m
  - Terraced Terrain Ranging: 0 - 1m
  - Able to withstand a load of 1.25N (for a robot of 500g assuming 4 wheels)
  - Able to travel at an average speed of 1m/s in these terrains
- Non-destructive or intrusive to the surrounding environment
- Non-toxic to the surrounding environment

Modelling Requirements

To effectively design the locomotive system for deformable terrain, various aspects of the problem need to be modelled to evaluate the performance of the design against the criteria mentioned above. These aspects can be split into terrain modelling, robot dynamics and the interactions between them. Hence, for the project, the modelling techniques used must be able to capture the following components:

- **Terrain**
  - **Deformable terrain (T1)**: Ability to capture the complex contact forces between the robot and deformable terrain, as well as within the terrain itself. This should capture the varying yielding nature of the surface as a function of the moisture of the granular composition (wet and dry sand).
  - **Topography (T2)**: Able to simulate the overall profile of the environment, including the maximum ascent, inclines and obstacles to overcome.
- **Robot**
  - **Kinematics (R1)**: Focuses on the overall movement and mechanics as a function of the robot's geometry.

  - **Materials (R2)**: Model and evaluate the structural integrity, including loads and failure points. Due to the use of soft actuators, large deformations and non-linear material dynamics need to be included in this model.

- **Computation**

  - **Integration & Versatility (C1)**: Ability to integrate outputs from one software or model and utilise it as an input to another. A single software won't be utilised for all elements of the design process, and hence multiple options will be used, which is why ease of use to integrate them is key. This includes its ease of use, licensing restrictions and documentation.
  - **Computational Power (C2)**: Resources required to run the model efficiently within a reasonable timeframe to obtain results, refine and improve the design.

It must be noted that despite the control strategy of a robotic system being a key part of the design process, this project aims to solely propose and focus on the novel design solution to the problem, and control is outside this scope.

Domain for Locomotion

The rugged deformable terrain domain being reviewed is inherently difficult to locomote through due to the terrain's characteristics being a function of moisture content. As expressed by Godon et al., they almost instantly deform under pressure with little recovery in shape [16]. Looking at soil as just one example, when the percentage of water is high it acts as a liquid, however, when that decreases soil is classified to have viscoelastic behaviour until a point that it is considered all solid [4]. Hence, the proposed design is aimed at the constantly yielding terrain found in abundance throughout the natural environment alongside the obstacles that are present alongside it.

1.2. Literature Review

Despite the large advances in robotics, locomotion remains problematic due to the yielding nature of the medium. Due to its non-homogeneous granular structure, it makes it difficult to generate a consistent tangential reaction force needed for locomotion. The motion utilised by animals to overcome the discussed terrain utilises a large amount of adaptation. For example, lizards are known to press their toes deeper into the more compact sand below the surface, crabs distribute their weight over eight legs and camels utilise its large surface area to compact the sand for a stable base [25]. Hence, from this, it is clear that adaption is a key aspect to the success of the design.

Robotic Mechanisms

With the advantages of an adaptive structure in this terrain and the need for a non-intrusive mechanism as per the requirements, soft actuators were chosen to be the base of the design and the point of research. Here, "soft" refers to materials with an Elastic Modulus similar to those found in nature (e.g., tissue and muscles) in the range of 10^4 to 10^9 Pa, compared to rigid components in the 10^9 to 10^{12} Pa range [35]. Although there is a significant body of research focused on bio-mimetic designs using soft actuators, its main aim is to understand animal kinematics and not design with an application in mind. For instance an eelworm-inspired tethered robot [30] using soft fluidic actuators (SFA) , a series of McKibben actuators mimicking snake-like motion [60], a frog-inspired jumping robot [58], or a turtle inspired robot with shape memory alloy wires being embedded into a polymer composite [24]. While innovative, these designs are often complex and remain tethered to laboratory settings due to the complex dynamics resulting in large power requirements, limiting their application potential. [22]. The most relevant non-intrusive and non-tethered example is from Tolley et al. with this multi-modal robot being tested in multiple real environments[44]. It proved successful in its aims and was able to lift loads up to 8kg however its overall velocity remained slow, and its unique design is difficult to incorporate into traditional robotic systems.

Instead, looking at kinematics as a starting point, Shui et al. looked at the most efficient forms of locomotion in soft robots. It was found that from the motions discussed in this paper, the efficiency is ranked in descending manner as follows: serpentine, rolling, paddling, undulation-based crawling, actinomorphic crawling, and peristaltic crawling [37]. Although serpentine-like motion scored the highest, its proximity to the ground means more complex actuation methods are required to go over obstacles. Instead, a large portion of research combined the second and third most efficient mechanisms (rolling and paddling) to create a cyclic paddler. A cyclic paddler is designed with a rotational centre (a wheel) to maintain a relatively high velocity with radially expanding limbs that aid in its ability to climb over obstacles. However, this design has only been utilised in the rigid domain and is yet to be explored with soft actuators. Examples include the SeaDog by Klein et al., the insect-inspired beach robot by Floyd et al. and other examples seen in Figure 1.1.

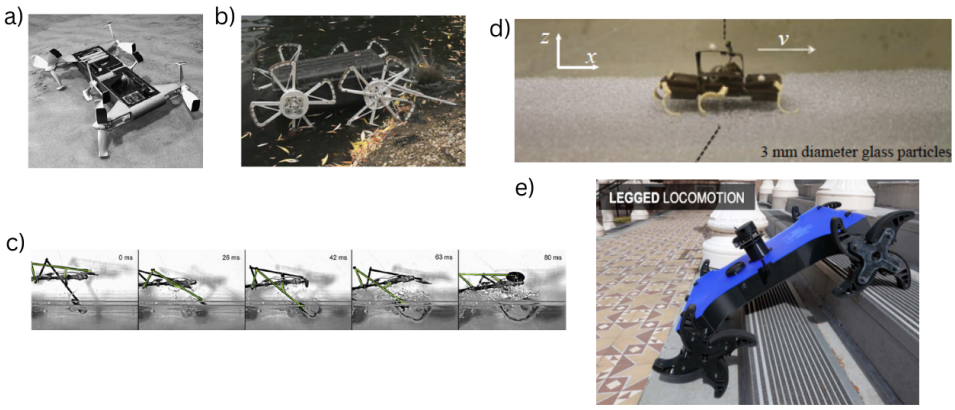

Figure 1.1: Different examples of robotics utilising cyclic paddlers a) Insect-Inspired Beach Robot [5], b) SeaDog for water and land mine detection [25] c) Basilisk Lizard inspired robot [12], d) DynaRoACH testing the benefits of ground fluidization [56], e) α-WaLTR with an adaptive wheel and leg transformation [57]

From literature research, it is clear that the easy integration of cyclic paddlers with existing robotic components (e.g. traditional DC motors) results in these systems more frequently being tested outside the laboratory environments than more novel actuation methods made from soft materials (such as the examples mentioned earlier). However, the existing cyclic paddlers are still made of rigid structures that may damage the surrounding environment and lack the ability to adapt.

Soft Actuators

Soft actuators in robotics come in many different forms due to their high elasticity. Common actuation forms include shape memory alloys, pneumatic artificial muscles and SFAs. Shape memory alloys are a group of materials that have an intrinsic material memory (also known as the shape memory effect), are lightweight and coupled with a high elasticity. These three properties mean that they have been explored extensively as actuators in soft robotics from medical applications [40] to grippers and underwater exploration robots [23] as the memory can be actuated and hence controlled under the stimulus of heat due to internal phase changes. Pneumatic artificial muscles consist of an elastomer channel surrounded by a braided mesh sleeve that is clamped on both ends to create a closed-off cavity. The conjunction of the 2 materials can mimic the movement of agonist-antagonist pairing seen in muscles, as the name suggests, allowing for both expansion and tension. When pressure is pneumatically supplied, a strain is created due to either the expansion or contraction in the radial direction of the elastomer channel whilst being restricted by the mesh sleeve. This results in an axial load, providing unidirectional actuation. Finally, SFAs utilise the high elasticity and low durometer of silicone-based polymers to design a structure with deliberate hollow chambers that are allowed to expand when filled with pneumatic or hydraulic pressure. This is then coupled with a strain limiting layer that acts as an inextensible constraint [46]. When pressurised in a spatio-temporal manner, the stiffness differential causes deliberate and controlled deformation, which is how an SFA provides an actuation force.

In comparison with pneumatic artificial muscles, SFA's have a lower actuating pressure (3-8 PSI vs 50-100 [26]) as well as a higher power-to-weight ratio (see Table 1.1). Likewise, although shape memory alloys are heavily utilised in bio-inspired robotics, they require precise temperature control to reduce fatigue and energy-dense power supplies if requiring fast actuation[51, 9, 59]. This makes the use of such actuators difficult to use in a dynamic outdoor environment. Material-wise, SFAs can be manufactured from siloxane-based polymers which are hydrophobic, resistant to ultraviolet light over several decades and fire-resistant [44], all making them suitable for exploration in outdoor environments. For the above-mentioned reasons, SFA's were chosen for the design process.

Actuator Type	Power/Weight [W/kg]
SFA	$10^2 - 10^5$
Hydraulic	$10^3 - 10^4$
SMA	$10^2 - 10^3$
PAM	$10^2 - 10^3$
Pneumatic	10^2
Electric	$10^0 - 10^2$

Table 1.1: Varying power-to-weight ratios of common soft and rigid actuators. [6, 31, 13, 17]

SFA's are commonly designed in 3 forms: i) pleated (also known as a PneuNet), ii) ribbed, iii) cylindrical [6] as seen in Figure 1.2. In its simplest pleated form, a stiffer inextensible panel on one side coupled with a series

of hollow channels made of the less stiff elastomer results in a unidirectional actuation. The actuation of the remaining 2 types is the same, with just the design incorporating more complex channels and members to achieve bidirectional and multi-directional actuation. As studied by Marchese et al. it was found that a pleated structure generates the highest tip force of the 3 configurations which is the reason for its choice in the proposed design [27].Examples of the various types of SFA being used in locomotive robots can be seen in Figure 1.3

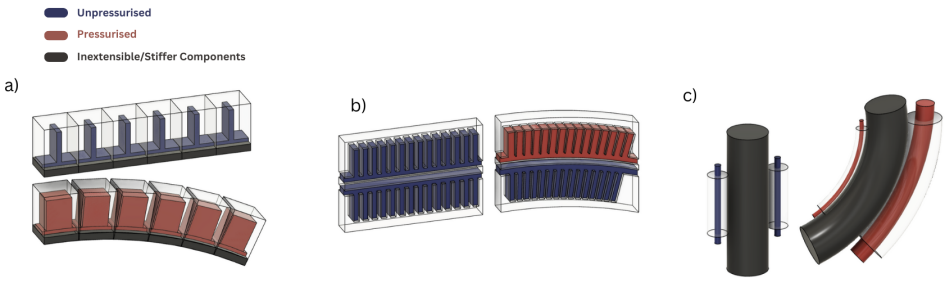

Figure 1.2: Schematic of the operating principles of an SFA a) Pleated, b) Ribbed, c) Cylindrical. Based on [26]

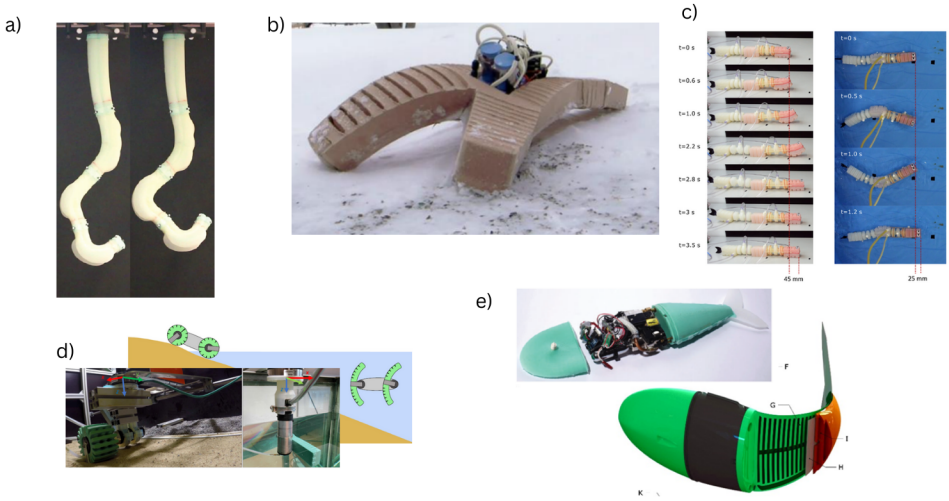

Figure 1.3: Range of soft robots that use SFA for locomotion a) Example of a cylindrical SFA gripper [29] b) Untethered multi-modal robot using a series of PneuNet SFA's [44] c) Eelworm inspired ribbed tethered SFA based robot [30] d) Tethered PneuNet SFA multiphase robot [15] e) Untethered robotic fish designed for quick escape manoeuvres using ribbed SFA's. [28]

Modelling Tools

To meet the modelling requirements set out, common tools, both commercial software and research-developed programs, were reviewed. Table 1.2 evaluates the available options and scores them according to their ability to fulfil the requirements (seen in section 1.1) based on functionality as well as the accuracy of the physics model used.

Model/Software	T1	T2	R1	R2	C1	C2	Total
VoxCAD [19]	1	2	2	3	2	4	14
MuJoCo	1	5	5	1	4	4	20
SoftZoo [50]	4	1	3	3	1	1	13
Unity 3D	2	4	4	2	1	2	15
Altair EDEM	5	2	2	1	4	3	17
Ansys Mechanical	1	1	2	5	3	2	14
Altair MotionSolve	1	1	5	1	4	3	15

Table 1.2: Evaluation of modelling options, scoring each software's ability to meet the requirements above. Scoring ranges from low performance to high performance, 1 to 5 respectively.

Using Table 1.2, the packages selected used for the design process are MuJoCo, Ansys Mechanical, and Altair EDEM coupled with Altair Motionsolve. MuJoCo's strength lies in its versatility and accuracy in the contact models for rigid body multi-body dynamics. With it being a robot-oriented physics engine that

runs on XML scripts, it is a very useful tool to iterate over numerous different geometric configurations and quickly test them over the various terrains due to the built-in Python bindings. MuJoCo's handling of joints is more computationally efficient than other physics engines as all bodies are assumed to be rigid with degrees of freedom being added versus the counter approach of subtracting freedom from free bodies [42]. In comparison, although Unity 3D provides similar capabilities to MuJoCo, its purpose is built with rendering efficiency in mind (i.e. for games) and not with kinematic accuracy. Hence, performing more complex physical interactions in Unity3D would come at a cost of computation time. Similarly, despite Altair MotionSolve being a traditional multi-body dynamics software and still useful, the interface means each small design change or modelling of the rigid obstacles and terrain has to be done manually. This makes the initial exploration of designs slow in comparison to MuJoCo where automation through code can be used. However, its high compatibility with Altair packages means it will still be used to evaluate the final design coupled with EDEM.

Looking at the tools from research that have explored similar goals of locomotion in deformable terrain through soft actuation, the use of VoxCAD and SoftZoo does seem initially promising. Softzoo does capture both the deformable terrain and soft actuation through the use of differentiable physics (which MuJoCo does not). However, it doesn't allow for any other terrain than flat, has an evolutionary design approach which is computationally heavy, and the documentation stops at the specific research goals, making it difficult to customise for other applications. Similarly, VoxCAD's main strength is the quick design and simulation of soft voxel-based robots on flat terrain. However, given the linear modelling approach of the voxel's deformation, the material characteristics would need to be still verified with traditional finite element analysis (FEA) calculations, making it more of an extra step than a design tool.

Thus, Ansys Mechanical's ability to accurately capture hyperelastic material models makes it a better choice compared to alternatives like VoxCAD and SoftZoo. While still computationally demanding, precise material deformation is critical to the design process. It's more advantageous to run detailed simulations on key sub-components than to simulate the entire system with oversimplifications and assumptions that could compromise accuracy. Finally, to accurately model the deformable terrain, the discrete element method (DEM) is able to capture the interparticle dynamics. With its easy coupling with MotionSolve, both Altair products provide a strong tool to determine the effect of the robot on the terrain and vice versa.

2| Design Framework

From section 1.2, it can be seen that while soft robotics has made significant strides, much of the research has focused on understanding animal kinematics instead of an application-based approach. This has led to tethered designs with complex actuation mechanisms. Similarly, the robots designed with environmental exploration in mind are rigid, potentially harming the surrounding environment as well as lacking the benefits that an adaptive design could bring. However, the use of a cyclic paddler (combining the kinematic benefits from rolling and paddling) has proven to be successful in overcoming obstacles whilst easily integrating with standard robotic components. This paper aims to bridge the gap by proposing a design that leverages the benefits of soft actuators known for their high strain tolerance and flexible nature—while maintaining the practical, application-focused mindset of traditional robotics with the starting point for the design being a cyclic paddler.

From Table 1.2 the necessary modelling tools (MuJoCo, Ansys and Altair EDEM coupled with Altair MotionSolve) were evaluated and selected for the project. The framework in which these were used to obtain the final design followed the iterative design approach outlined by Roozenburg and Eekels in 1995 which can be seen in Figure 2.1.

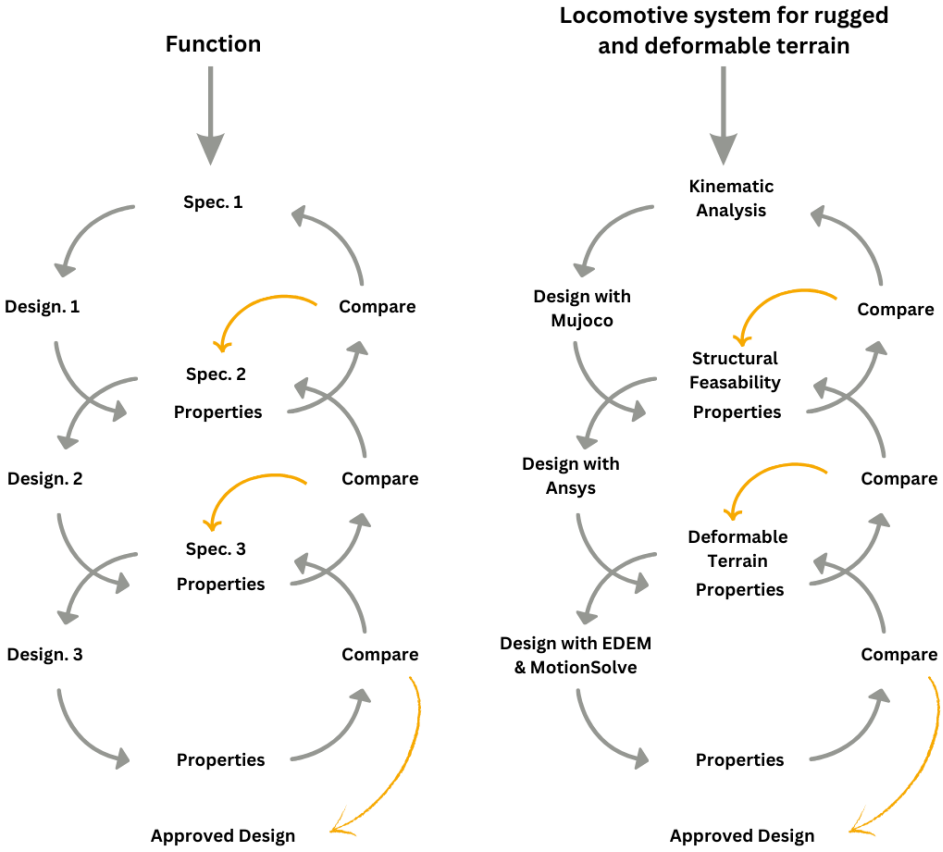

Figure 2.1: Iterative design cycle for project adapted from [48]

The report follows the structure of the design cycle starting with a kinematic analysis using MuJoCo to test how different design parameters (number of paddles and shape of paddles) affect its ability to overcome varying obstacles in chapter 3. The scientific conclusions from this point were used to make informed decisions on the initial soft robotic design in chapter 4. Ansys Mechanical is then used to evaluate and improve the structural feasibility of the soft structure in chapter 5. The final design is then evaluated by modelling its behaviour in deformable terrain using Altair EDEM and MotionSolve as seen in chapter 6 before discussing the advantages, limitations and future work in chapter 7.

3| Kinematic Analysis

3.1. Methodology

Terrain Setup

A series of experiments were run to evaluate the effectiveness of different cyclic paddler configurations to locomote through rigid terrains of varying topography. The varying topographies include flat surface, ramped incline, ramped steps, smooth undulation, terraced undulation and obstacles as seen in Figure 3.1 with gravity present in the model of each terrain and varying shades of green to purely emphasise the height variation.

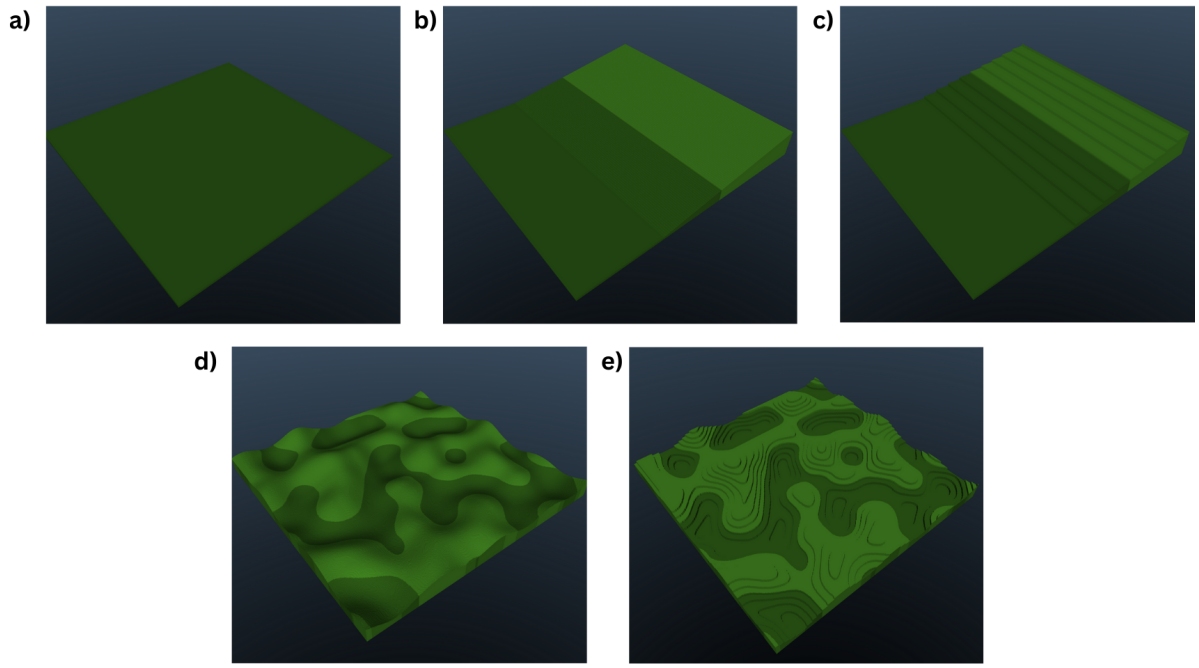

Figure 3.1: Different terrains used to test cyclic paddler configurations a) Flat Surface, b) Ramped Incline c) Ramped Steps d) Smooth Undulation e) Terraced Undulation

To generate the terrains, greyscale images were created in Python to represent the topography. Black pixels indicate the lowest points, white pixels the highest, with a linear gradient for everything in between. This is then extrapolated into a 3D surface mesh by using the height field function in MuJoCo providing the X, Y, and Z extremities of the terrain, of which an example can be seen in Figure 3.2. For each terrain, the robot is able to move through a 2500m^2 area (50 x 50m) with the height being a function of the type of terrain and experiments to be conducted as seen in Table 3.1. The 2 more complex terrains mimic a whole environment instead of a single task to be completed (e.g. going up an incline) as seen in Figure 3.1d and Figure 3.1e. This is achieved by creating an undulating terrain, with one having smooth variations and the other a terraced effect. To create such a greyscale image, Perlin noise was utilised to generate a noisy image that can then be utilised for the same height field function. It is one of the standard techniques for procedural terrain generation, as it generates a pseudorandom gradient vector at each grid point across a 2D plane to generate a realistic terrain image. Despite appearing random, by controlling inputs to the noise function, the level of undulation or number of terraces can be controlled to determine the frequency of obstacles the robot has to overcome. Perlin noise is fast and of higher quality in comparison to other common procedural terrain generation techniques such as midpoint displacement or diamond square, whilst being easy to implement using the noise module within Python [3]. The parameters used to define the Perlin Noise function (such as scale, octaves, persistence, lacunarity and seed) were used to ensure the terrain generated was identical each time and looked as realistic as the desired rugged terrain. For the entire set of values, see section 8.1.

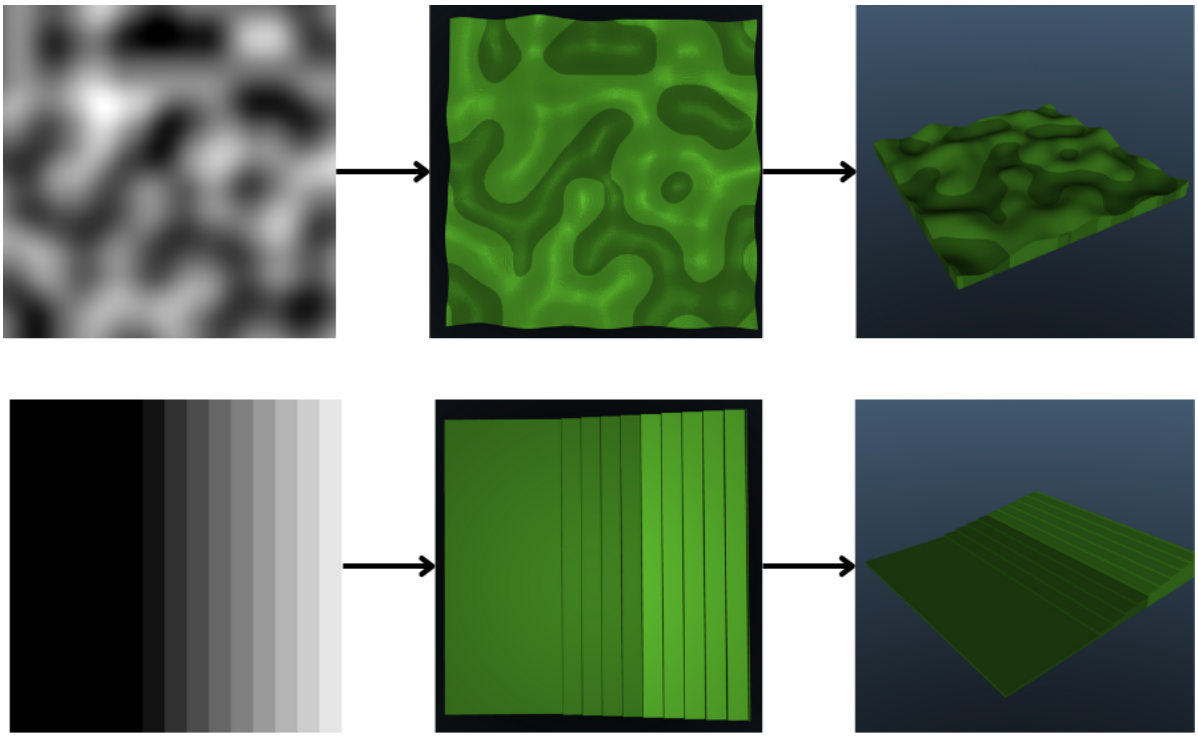

Figure 3.2: Conversion of greyscale image into 3D height field mesh

No.	Terrain	Elevation Change (m)	Feature
a	Flat Surface	0	NA
b	Ramped Incline	2.1	17.5°
c	Ramped Steps	2	10 Steps
d	Smooth Undulation	1	Perlin Noise
e	Terraced Undulation	1	Perlin Noise & 8 Terraces

Table 3.1: Key parameter settings for different terrains

For all terrains, the robot was placed in front of the main obstacle (e.g. the slope) beside terrains d and e from Figure 3.1. The location in which the robot is placed may affect its performance due to the random nature of the terrain. Due to this, for those 2 terrains only, the robot will be randomly dropped 3 times and the results averaged accordingly.

Robot Setup

With the terrain parameters set, the robot itself must be modelled in MuJoCo.To test various cyclic paddlers, the body of the robot remains constant as a box to which 4 cyclic paddlers could be attached. The box was modelled in Fusion360 with 'eyes' to differentiate if the robot was going forward or backwards and exported as an STL file. The advantage of this approach meant that a new paddler could be quickly tested by superimposing a new STL file of each cyclic paddler using code onto the body and running it through the same terrains and tests.

This body in MuJoCo has a free joint (allowing 6 degrees of freedom) attached to it to allow it to roam through the terrain and be under the influence of gravity, alongside 4 hinge joints (1 on each corner for each cyclic paddler, see Figure 3.3). A hinge joint is between 2 bodies where there is only 1 degree of freedom about a rotational axis (such as a wheel). To ensure a stable rotation, a damping coefficient of 0.05 was introduced to each joint. The 4 cyclic paddlers that are connected through the hinge joint are structured in the XML file as a child of the robot body. This is crucial as that means that the simulation will only check for friction and contact between the entire robot and the terrain and not between child and parent bodies. This reduces the computation time significantly, and the exact details of bearing loads or axial frictional losses are not of concern in this stage of the design process.

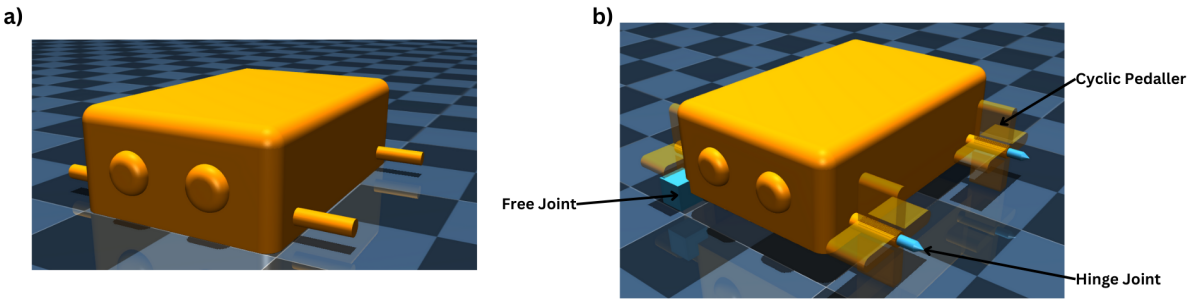

Figure 3.3: a) Main robot body for MuJoCo Simulation b) Main robot body with 4 hinge joints, free joint and example cyclic paddler

For the set of experiments, the cyclic paddlers tested were as follows: single straight leg, double straight leg, triple straight leg, quadruple straight leg, single curved leg, double curved leg, triple curved leg, quadruple curved leg and a wheel (to be seen in Figure 3.4). The radius of each design is kept the same so that purely the effect of the number of paddles on each wheel and the shape of the paddles are being tested. A standard wheel was included in the experiments as a control for comparison.

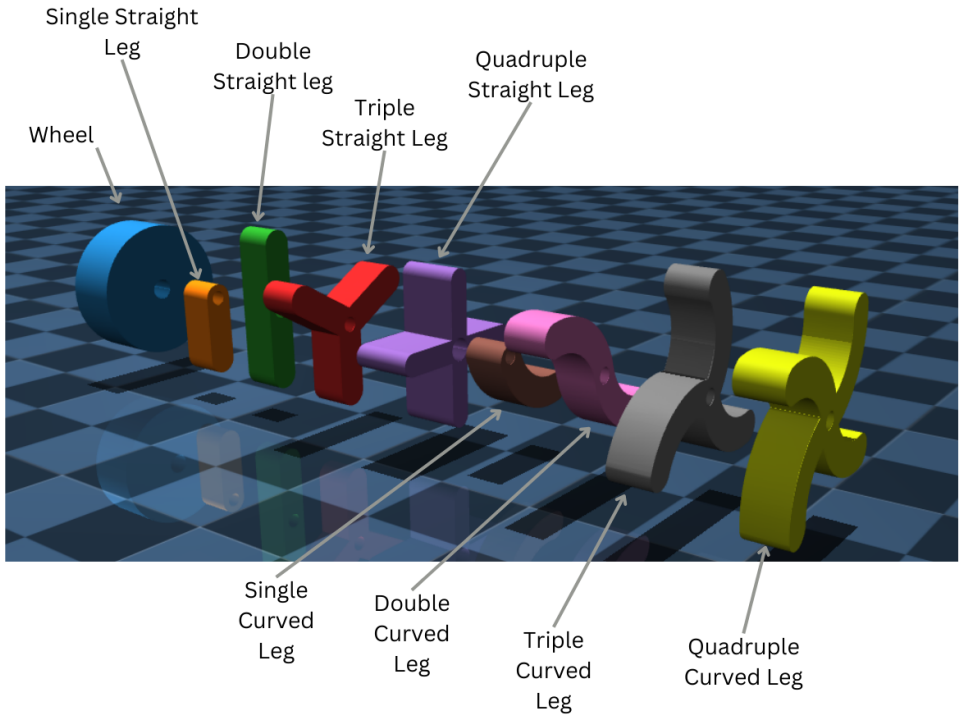

Figure 3.4: Range of cyclic paddlers

Experimental Setup

With the robot and terrain parameters modelled, the following experiments could be setup. To ensure that the experimental parameters remain purely geometric, the control strategy to each wheel and therefore each robot is identical. Initially, no movement is applied for the first 0.5s to allow the robot to fall into the environment and reach a steady position. From here a gradually increasing rotational velocity (over 1 second), levelling off at $2\pi rad/s$ was applied to each hinge joint. For this, a velocity servo is added to each hinge joint that has a basic proportional differential controller to try and maintain a steady desired value. This was chosen over a torque servo as if a wheel is not in contact with the ground, the wheel accelerates indefinitely, making either the robot or the simulation unstable.

The final addition to the model is to set the friction coefficients between the robot and the terrain. The friction is set as a property of the robot geometry, defining the coefficients of friction as well as the dimensionality of the contact space in which the model checks for contact between two geometries. The dimensionality (set using the Condim variable) was set to 3 applying regular frictional contact and opposing slip in the tangent plane. The default time step was used 0.002s, as this favours stability and accuracy over the model's efficiency. For the coefficients of friction, the exact material to be used for the design is unknown until having performed the structural validation experiments in chapter 5 as well as getting exact values for a unique material requires extensive experimentation. Instead, values from a tyre sand interaction from the literature were used as an

approximation [52]. This is because the actuation method is known to be soft, meaning the material will be rubber/silicone-based and the terrain intended is deformable. From this, the friction parameters were set as follows:

$$\text{Sliding Friction} = \mu_s = 0.6 \tag{3.1}$$

$$\text{Torsional Friction} = \mu_t = 0.005 \tag{3.2}$$

$$\text{Rolling Friction} = \mu_r = 0.2 \tag{3.3}$$

The total number of simulations to be run in MuJoCo was 81 accounting for the 9 wheel designs, all terrains, and the repeats on the smooth and terraced terrain. Each simulation was run for 10.5 seconds, with the distance travelled measured as the metric for comparison. This distance is taken from a 'framepos' sensor added to the centre of the robot body that records its Cartesian coordinates during the simulation. The distance travelled will be calculated using Euclidean distance between the starting point and its current point in the simulation as follows:

$$d = \sqrt{x^2 + y^2 + z^2} \tag{3.4}$$

The distance travelled (d) alongside a video of the simulation is recorded to evaluate the success of each design and which design to take forward.

3.2. Results

With all 81 experiments run, both quantitative (from the data) and qualitative aspects (from analysing the simulation videos) were used to inform the decision of the final geometry.

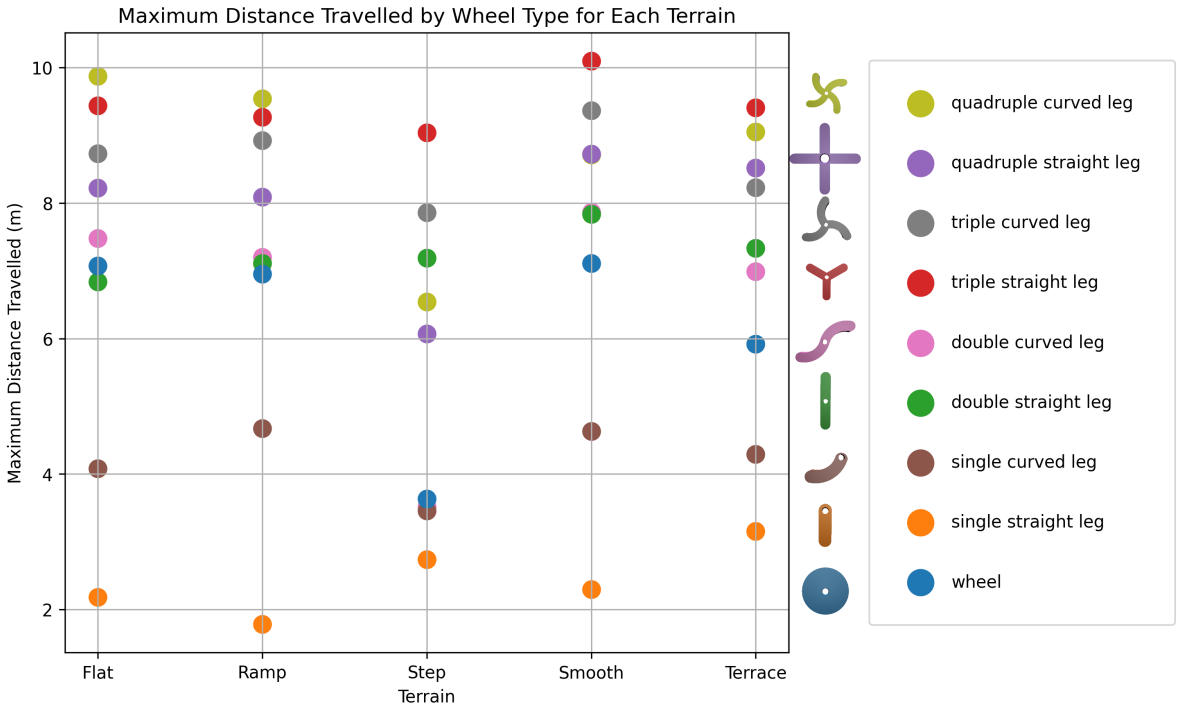

Figure 3.5: Maximum distance travelled by each wheel type under each terrain

From looking at the maximum distance travelled by each wheel on each terrain (as seen in Figure 3.5), 3 key points of analysis can be seen. It must be noted that for the smooth and terrace terrains, the values are an average of 3 experiments where the robot was dropped randomly each time. The first main conclusion is that the designs that had multiple limbs (triple and above) performed better than those with single or double limbs. The second conclusion is that the control (a wheel) still performs comparatively to the other designs, despite being on a stepped terrain. The third conclusion is that curved or straight legs are advantageous depending on the terrain. Curved legs performed better on flat and ramped surfaces, whereas straight legs are more suitable for the remaining terrains.

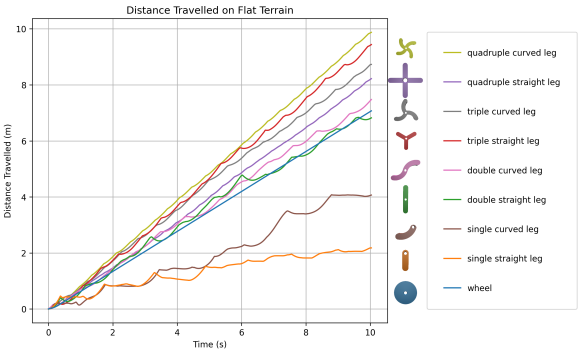

(a) Distance travelled by various wheel designs on flat terrain.

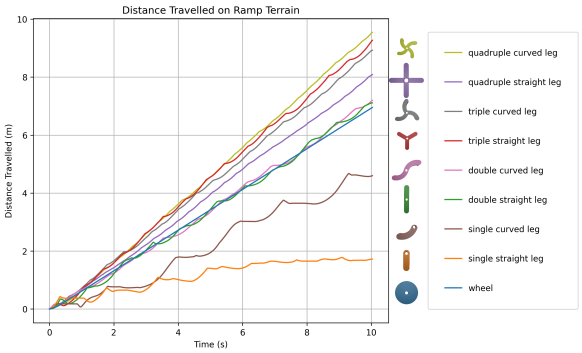

(b) Distance travelled by various wheel designs on ramped terrain.

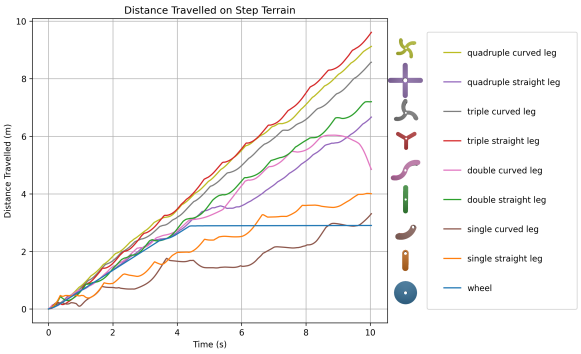

(c) Distance travelled by various wheel designs on stepped terrain.

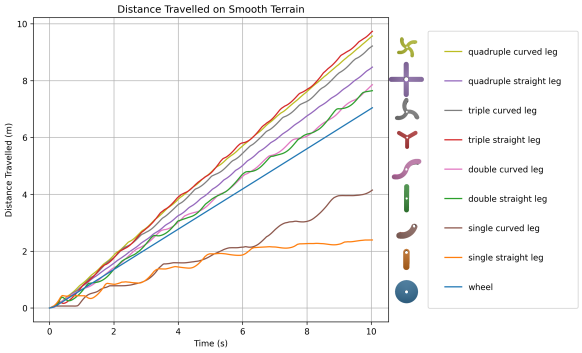

(d) Distance travelled by various wheel designs on smooth, undulating terrain.

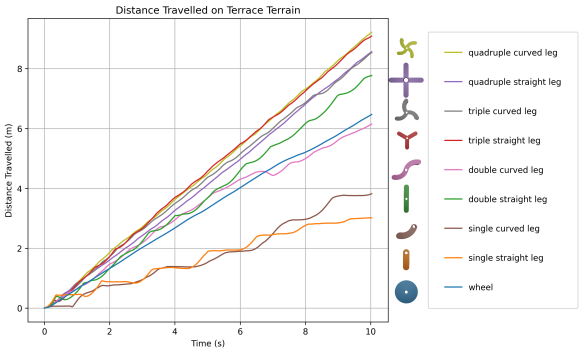

(e) Distance travelled by various wheel designs on terraced undulating terrain.

Figure 3.6: Distance travelled by various wheel designs on different terrains.

If looking further at the movement of the robots throughout the simulation (see Figure 3.6), it can be seen if the robot got stuck, and the characteristics of the motion on each terrain. The first notable point is that designs with more limbs tend to maintain a more constant speed, as reflected in the more linear relationship due to the increased contact area with the ground. This reduced the overall slip of the design, making it more efficient in its locomotion.

Looking more closely at Figure 3.6c, it can be seen that the wheels could not overcome the steps due to the plateau in displacement. When reviewing the simulation, the robot's dimensions were such that the body was left idle on the corner of the step, meaning no wheels were in contact with the ground (with an example of this to be seen in Figure 3.7. This was not the case with designs of more than 3 limbs.

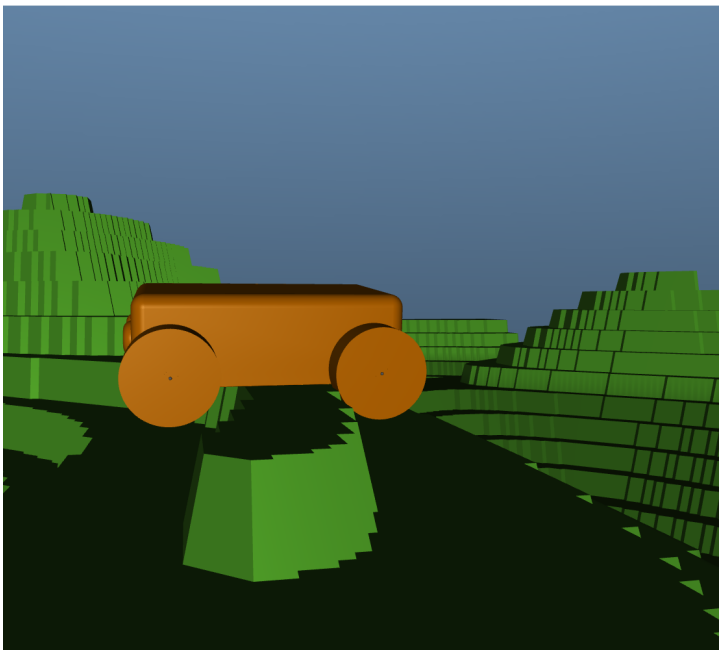

Figure 3.7: Wheel design being beached due to terrain topography

With the data indicating clearly which designs were most successful, analysing the simulation videos helped to understand why that is the case and which components are important, as well as the aspects that weren't captured in the data that proved to be significant. From here, it was clear that the contact area and stability both played a significant role in the success of a design. Contact area affected how much of the applied torque was converted to a forward motion, resulting in the triple and quadruple-limbed designs travelling further than the single and double designs. Stability affected its ability to move in the first place. Given the slopes and steps throughout the terrains, the initial placement of the robot in the environment heavily affected its performance. The structure in the designs of 3 limbs and more meant that no matter how it landed, there was always a component in contact with the terrain. Analysing the footage of the double-curved design on the stepped terrain, shows it tipping over itself, explaining the negative displacement at the end of Figure 3.6c. In other single and double-legged designs, problems such as 1 limb facing a completely different direction from the other 3 due to the terrain result in requiring a much larger torque to overcome its weight and generate locomotive motion. In certain cases, however, the asymmetry was in favour of the locomotion, reducing the chance of the body getting stuck.

With all models, this simulation using MuJoCo had simplifications that need to be considered in this analysis. The terrain for the robot to move across was entirely rigid. Hence, although the friction coefficients were selected to mimic that on deformable terrain, the contact area in the simulation versus reality is less. This is because there is no modelling of the robot 'sinking or digging' into the ground, meaning a successful design for rigid ground may have characteristics that are not favourable for deformable terrain. With the uncertainty of the terrain, it means that the single control strategy used may not be suitable for all. When analysing the videos, there were many cases where it was clear that a constant torque for each wheel was not suitable and hindered the locomotion. An individual drive for each wheel (and even better each limb) would have been advantageous to push itself out of a ditch or climb up an angled plane. This was a clear avenue for further exploration in all the designs, besides the control. An example of such a situation when individual drive would be needed with different torque and control strategies for each wheel can be seen in Figure 3.8. From the simulation videos, it was seen that its ability to upright itself, when knocked over, is more important than being able to move quickly across a terrain. This would be even more important in the real world, as disturbances such as animals or weather would be present.

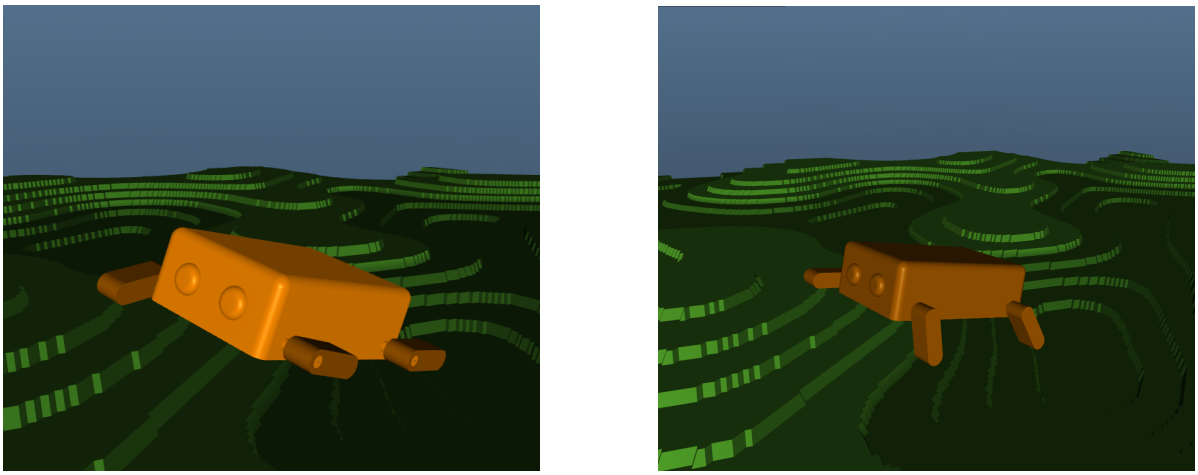

(a) Control & Torque Configuration 1

(b) Control & Torque Configuration 2

Figure 3.8: Different possible wheel configurations to overcome topography

Overall, from the kinematic analysis, the following conclusions were made to inform the parameters for the new design. The stability of a wheel design is crucial as it increases the probability that all 4 wheels are in contact with the ground. The introduction of limbs or symmetrical extending paddles increases its ability to climb on different terrains, with a larger number of limbs being favourable. The shape of the limb (curved or straight) proved advantageous in differing terrains, indicating that adaption is a key aspect of the design moving forward. In comparison, a wheel can only overcome a step (or similar obstacle), if it has sufficient momentum or is sufficiently large in comparison. Hence, although this project does not explore the optimal control strategy, a system that can mechanically change its shape gives more options for adaptive control strategies.

4| Design Concept

With the design goals in mind and the quantitative and qualitative design conclusions gathered from chapter 3 the proposed design is as follows. A completely soft wheel with 4 limbs (a cyclic paddler) where each limb is made up of inflatable hollow chambers as seen in Figure 4.1. The individual limb design is based on common SFA's which couples the inflatable hollow chambers with a strain-limiting layer on one side. When pressurised in a spatio-temporal manner, the stiffness differential causes deliberate and controlled deformation in one direction. This controlled deformation allows the wheel to adjust its curvature and height. Due to its highest tip force (in comparison to ribbed and cylindrical[27]), a pleated structure was chosen for the proposed design.

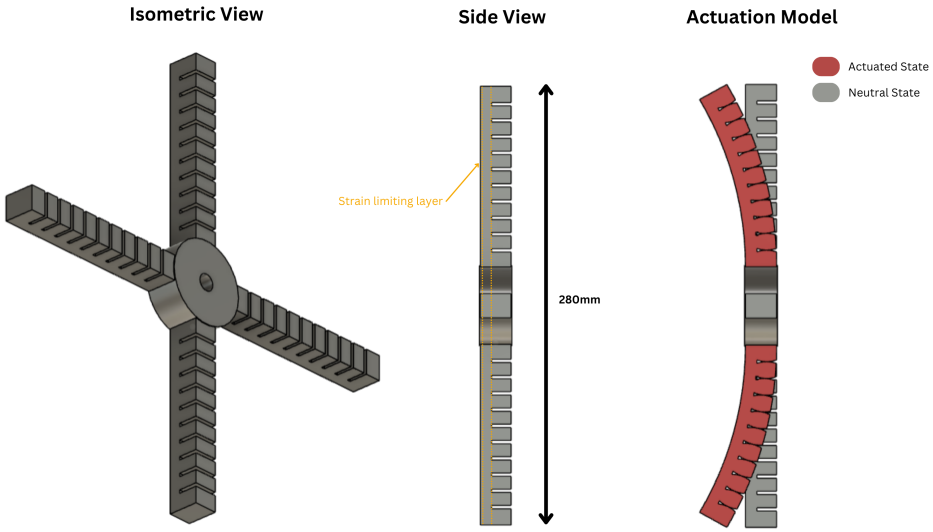

Figure 4.1: Proposed design concept of adaptive wheel

This design aims to maintain the overall advantages of wheel-based locomotion, whilst being able to change the curvature and overall height of the wheel to become significantly more adaptable in rugged terrain. By doing so, a robot could both climb over obstacles by having its limbs in an extended fashion and go under gaps by inflating the limbs to their highest curvature. The design can have a maximum diameter of 280mm depending on the inflation and form. It would also allow it to change the contact area with the ground, making it less prone to sinking in deformable terrain. This was the starting design after the first design loop from the Figure 2.1 going into the structural feasibility analysis.

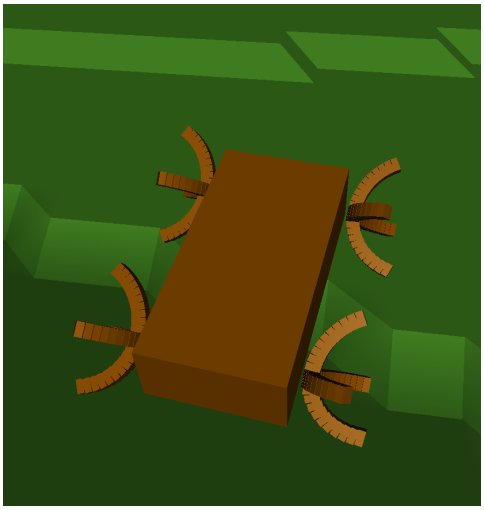

Figure 4.2: Proposed design concept of the adaptive wheel in MuJoCo environment

5| Structural Feasibility

5.1. Ansys Model Setup

Up to this point, the proposed design has only been simulated as a series of rigid bodies to test various prototypes of the design. However, the design is intended to be built out of soft materials, meaning this simulation doesn't capture many aspects of the material dynamics. For this, Ansys Mechanical as an FEA software was used to evaluate the structural feasibility alongside an analytical solution for verification. The procedure outlined below was then repeated each time an improvement or change was made in the design until all conditions were satisfied.

Model Simplification & Load Configurations

For the simulation, a static structural analysis of a hyperelastic material was run. The nonlinear nature of these materials means the computational power required is higher than an already computationally heavy FEA analysis on a rigid body. Due to this, the model being run in Ansys Mechanical was both geometrically and dynamically simplified. Geometrically, the part that is of main interest is the limb that is in contact with the ground as seen in Figure 5.1. It is the area that experiences the highest set of loads and the component that needs to support its self-weight. With this, only a quarter of the design is being simulated in Ansys Mechanical, reducing the number of mesh elements that need to be solved and hence reducing the computation time.

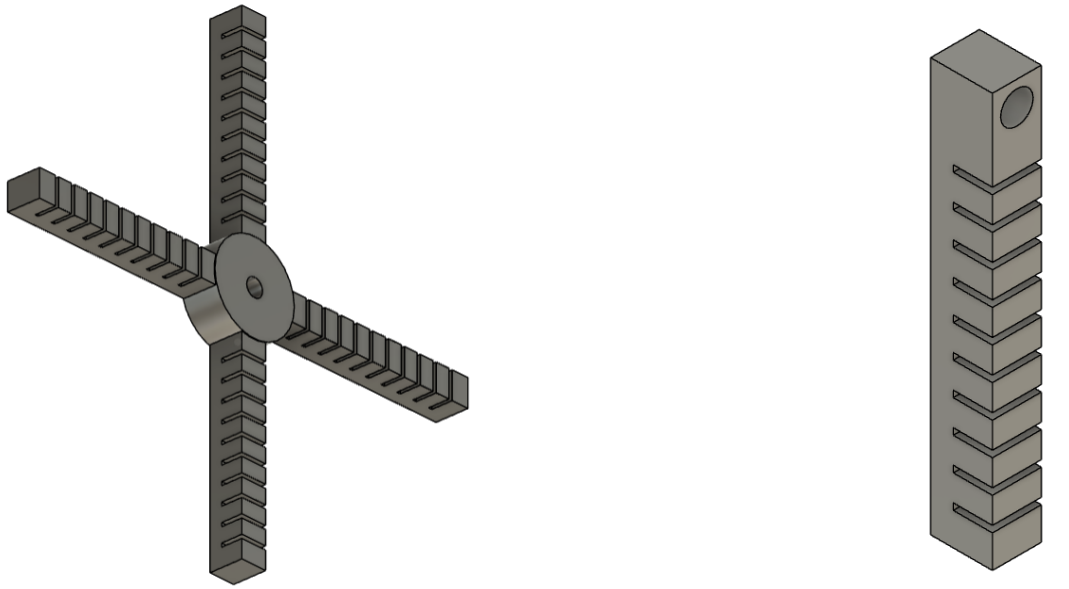

(a) Original Model **(b)** Simplified Model

Figure 5.1: Geometric simplification of the model for Ansys Mechanical

Dynamically, the model has been simplified by only including a quarter of the self-weight of the robot (assuming 4 wheels) and loading this contact force at discrete limb configurations. With this comes 2 key simplifications that must be noted when later analysing the results. Firstly, by including the self-weight (contact force with the ground) as the only external force, we are neglecting any torsional or perpendicular forces that are propagated through the structure when accelerating the robot forward. This simplification was made as the more complex the loading step, the larger the number of substeps and mesh details required to ensure convergence is still met in the solution. After some preliminary test simulations, magnitudes upwards of 10,000 substeps were still not sufficient to achieve convergence due to the sensitivity of the hyperelastic solver. The second simplification of only analysing discrete configurations is due to the change in contact area with the ground. As the system inflates or deflates to overcome a different obstacle or terrain, the area that is in contact with the ground (and supporting the self-weight) changes significantly. Hence, instead of simulating this entire sequence, the system is pressurised to a certain configuration before applying the

contact force to the corresponding points. By performing separate discrete loading configurations (LC) , the simulation can remain computationally efficient whilst testing the key modes of operation. Each design contains a fixed support boundary condition at the axle to generate the necessary reaction forces throughout the structure. The first configuration (LC1.1) is to characterise the system and capture the relationship between internal pressure and bending angle, which is then used for verification in section 5.2. The second configuration includes acceleration due to gravity to extract the pressure that needs to be applied to get the desired bending geometries.

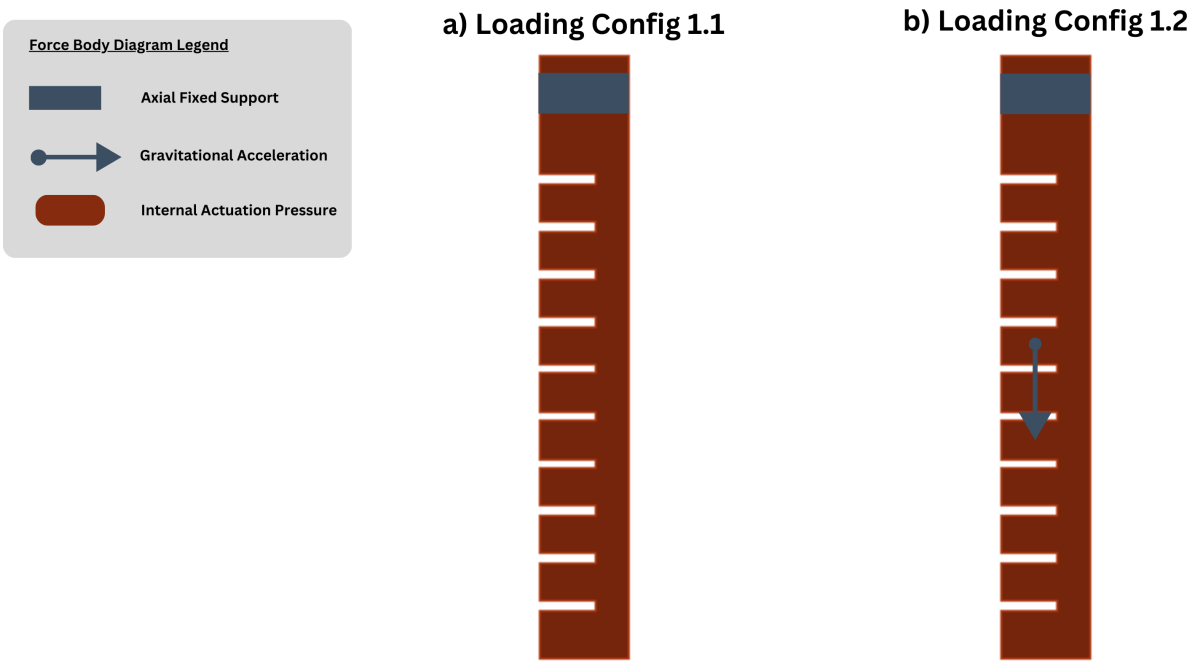

Figure 5.2: LC1.1 & 2, a) Internally applied pressure b) Internally applied pressure & gravity

From here 3 bending geometries are selected to test the design at critical points. For each case, the chambers are pre-pressurised to obtain that geometry before applying the contact force. The first is at a neutral position, hence no initial pressure being applied. This is followed by a partial bending and full configuration as seen in Figure 5.3. The numerical input values for each LC can be seen in Table 5.1. Each load was applied using a ramp function in Ansys to aid convergence and infeasible large deformations. For more information on the loading setup in Ansys, see section 8.3.

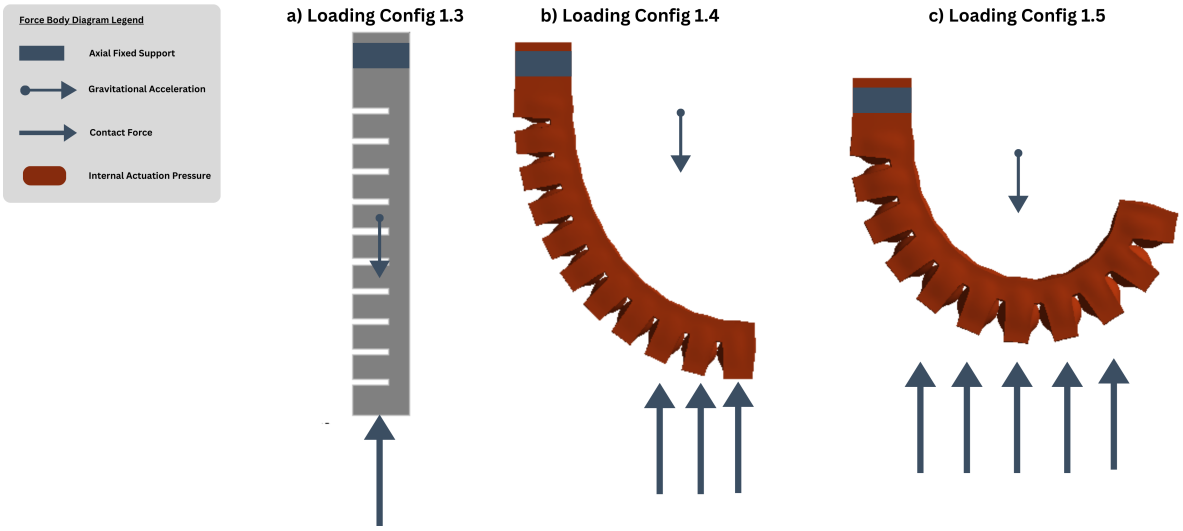

Figure 5.3: LC1.3,4 & 5, a) Loading at neutral position, b) Loading at partial bending, c) Loading at full bending

LC	Applied Pressure (kPa)	Gravitational Acceleration (m/s^2)	Contact Force (N)
1.1	40	0	0
1.2	40	-9.81	0
1.3	0	-9.81	1.25
1.4	29	-9.81	1.25
1.5	47	-9.81	1.25

Table 5.1: Input values for all LC's for the initial design

Mesh Settings, Timesteps & Contact Model

When setting a suitable mesh sizing with hyperelastic material models, a balance needs to be found between facilitating convergence (using a coarse mesh size) and still capturing the large deformation of each chamber (using a finer mesh size) as found by Tawk and Alici [41]. From analysing literature of similar-sized SFAs (50-200m length and 10-25mm width), a mesh size of 3mm was selected alongside linear order elements [53]. The number of load steps used was dependent on the LC however all simulations were run for 2 seconds for consistency. If a contact force was added, this was done in a new load step to avoid contact issues. For example, in LC1.4, the pressure was ramped up from 0 to 1 seconds to achieve the desired configuration and the external load was added in a second load step from 1 to 2 seconds to aid convergence. Within each load step, the load was applied ranging from 10-1000 substeps. This range allows Ansys to more gradually apply loads to ensure the contacts and deformations are captured while placing an upper limit to ensure a reasonable solving time.

For the deformation of each chamber to translate to a bending of the whole structure, Ansys needs to know which walls it needs to detect if they are in contact. A frictional contact was set between all outer walls between the chambers with a coefficient of 0.2 as seen in Figure 5.4.

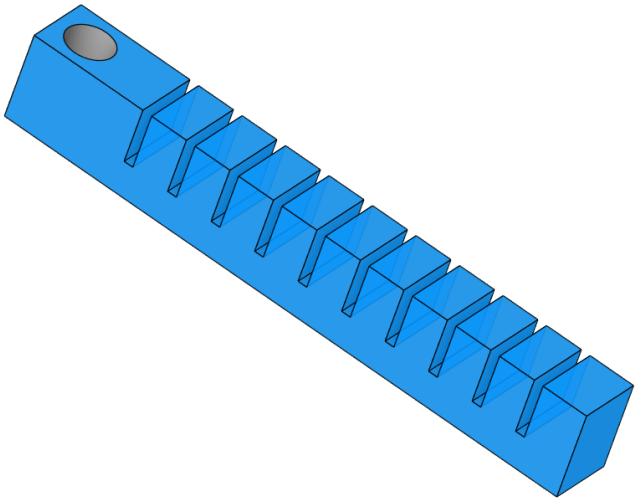

Figure 5.4: Planes between chambers selected for contact model

Material Selection

The material selected for the analysis was Dragon Skin 30. A large range of materials have been used for soft actuators, with silicone-based polymers being the primary choice due to their high maximum strain value [47] and being non-toxic to the surrounding environment. Common variants of silicone include Ecoflex, Smooth-Sil and the Dragon Skin series[8, 33, 11, 55, 36, 45]. When selecting the material, both shore hardness and the stress-strain response were taken into consideration. Shore hardness is a measure of how resistant the material is to indentation. With the goal being to use this design in rugged and deformable terrain, a higher shore hardness increases its lifespan by reducing the chance of puncture and general wear and tear. Of the commonly available silicone variants, the Smooth-Sil series has the highest shore hardness, followed by Dragon Skin and Ecoflex [53]. The stress-strain response affects the stiffness of the material and with that the power requirement for a pneumatic system to actuate the design and more importantly the ability to withstand the loads and large deformations without failure. Hence, despite the high shore-hardness, the Smooth-Sil series has a low strain failure in comparison with the others ranging from 100% to 250% [10, 34] in comparison to 300% and 500% for Dragon Skin and Ecoflex respectively [38, 14]. Hence, the elastomer with the highest shore hardness of the Dragon Skin series whilst maintaining a high strain failure rate (Dragon

Skin 30)[1] was selected.

Due to the nonlinearity in elastomers, a hyperelastic model must be used to characterise the stress-strain response. Various strain energy functions (Ψ) are used within Ansys where the coefficients of the function can be set to best fit the experimental data of the response. For Dragon Skin 30, it was found that a 2nd-order incompressible Yeoh Model was most suitable to capture the stress-strain response, as it's suitable for large strain problems at or above 400% [53]. This model (as well as the analytical) was utilised for all Ansys simulations throughout the iterative design problems.

$$\Psi = C_1(I_1 - 3) + C_2(I_1 - 3)^2 + C_3(I_1 - 3)^3 \tag{5.1}$$

Reducing down for the 2nd order model as follows:

$$\Psi = C_1(I_1 - 3) + C_2(I_1 - 3)^2 \tag{5.2}$$

The strain energy function can then be expressed as a stress-stretch relationship for a uniaxial tensile loading as follows [53]. Although the loading experienced is more accurately represented with a biaxial model, there is no data available for the biaxial loading of Dragon-Skin 30 and hence uniaxial has to be used.

$$I_1 = \lambda_1^2 + \lambda_2^2 + \lambda_3^2 \tag{5.3}$$

$$\lambda_i = \frac{l_i}{L_i}, \quad i \in \{1,2,3\} \tag{5.4}$$

Where:

- Ψ is the Strain Energy Function
- C_1, C_2, C_3 are material constants
- $C_1 = 114.88kPa$ [54]
- $C_2 = 1.262kPa$ [54]
- I_1, I_2, I_3 are the principal invariants
- λ_i are the stretch ratios
- l_i is the deformed length
- L_i is the undeformed length

Once the design has gone through all load cases, the results are analysed to determine the maximum strain, maximum true stress, bending angle and overall deformation profile. The maximum stress and strain are to be used to determine if the design has experienced material failure and uneven pressure distribution. Material failure for Dragon Skin 30 occurs at a true stress value of 34MPa and strain of 700% with the full experimental uniaxial stress-strain relationship in which the Yeoh model is fitted upon seen in Figure 5.5. The bending angle is determined by adding a probe on the end face that captures the average Eulerian angle with respect to its original position. The deformation profile allows us to visually inspect the design weaknesses as well as to understand operational characteristics as the contact force is applied. Once the analysis of the first design is complete, the design is improved and the same set of simulations are run until the final feasible design is obtained.

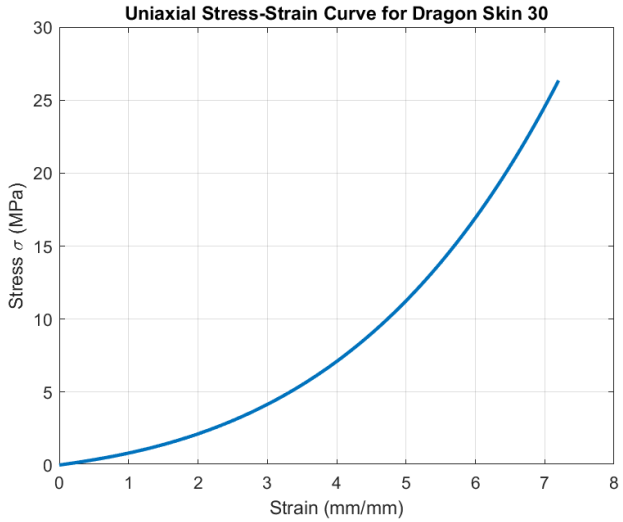

Figure 5.5: Stress strain response for Dragon skin 30 under uniaxial tension, adapted from [54]

5.2. Analytical Model Setup

To verify the Ansys model (LC1.1), an analytical model was developed alongside the FEA simulation. The analytical model is based on the principle of minimum potential energy (Γ) applied to an individual soft chamber. This can be defined as the sum of the internal material strain energy (U) and the work potential (W_p) , This model builds on the approach proposed by Cao et al. [7].

$$\Gamma = U + W_p \tag{5.5}$$

As work is being done on the system (in this case pressure), it is assumed that the deformation caused is perfectly elliptical, resulting in an overall uniform curvature of the actuator as seen in Figure 5.6.

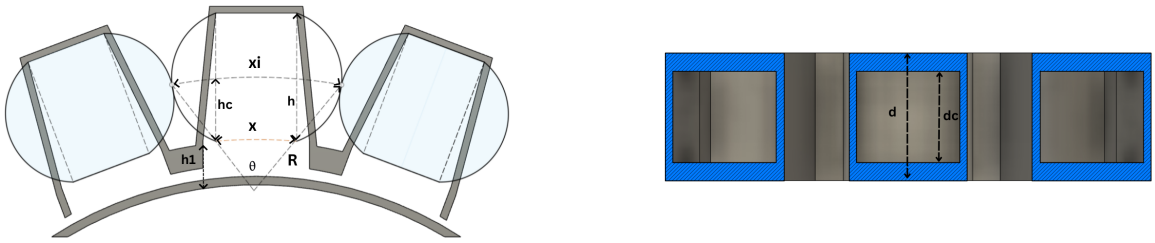

(a) Cross-Section View

(b) Top View

Figure 5.6: Schematic and geometry of the inflated chambers

From this, the following geometrical relationships can be made:

$$\theta = \frac{x_i}{R} = \frac{x}{R - h_c} \tag{5.6}$$

$$k = \frac{1}{R} \tag{5.7}$$

$$V_i = \frac{\pi}{4} h x_i d_c \tag{5.8}$$

Where:

- subscript i refers to the property when inflated
- θ is the bending angle.
- R is the radius of curvature.
- x is the original chamber width.
- x_i is the maximum inflated chamber width to be found at the centre of the ellipse.
- h_c is the distance to the centre line of the ellipse.

- h_1 is the distance from the base of a chamber to the top of the strain-limiting layer
- h is the total height of a chamber.
- k is the curvature.
- V_i is the inflated volume of a chamber.

By combining eqs. (5.6) to (5.8),the inflated volume can be expressed as follows:

$$V_i = \frac{\pi}{4} h \frac{x}{1 - k h_c} d_c \tag{5.9}$$

Expanding Equation 5.5, it can be expressed as the internal strain energy of one chamber minus the work done due to the applied pressure to that chamber.

$$\Gamma = \frac{1}{2} D k_i^2 x_i - P_i V_i \tag{5.10}$$

$$D = EI \tag{5.11}$$

$$I = \frac{d h_1^3}{12} \tag{5.12}$$

where:

- D is flexural rigidity.
- E is elastic modulus.
- I is the moment of inertia of the chamber.
- P_i is the inflation pressure.

However, due to the hyperelastic material properties, the elastic modulus cannot be constant and instead is a function of the strain. Using Equation 5.1, the uniaxial stress-stretch relationship can be obtained as follows [53]:

$$\sigma = 2\left(\lambda^2 - \lambda^{-1}\right)\left(C_1 + 2C_2\left(\lambda^2 + 2\lambda^{-1} - 3\right)\right) \tag{5.13}$$

$$\lambda = \epsilon + 1 \tag{5.14}$$

$$\sigma = 2\left((\epsilon+1)^2 - (\epsilon+1)^{-1}\right) \cdot \left(C_1 + 2C_2\left((\epsilon+1)^2 + 2(\epsilon+1)^{-1} - 3\right)\right) \tag{5.15}$$

where:

- ϵ is the strain

From Equation 5.15, the gradient can then be used as a function of strain to accommodate for the non-linearity. From here, eqs. (5.10) and (5.11) can be combined to get the following expression:

$$\Gamma = \frac{EI k_i^2 x}{1 - k_i h_c} - \frac{\pi P_i h x_i d_c}{4} \tag{5.16}$$

The point of equilibrium can then be found by solving $\frac{\partial \Gamma}{\partial k} = 0$:

$$\frac{d}{dk}\left[\frac{EI k_i x}{1 - k_i h_c} - \frac{\pi P_i h x_i d_c}{4}\right] = 0 \tag{5.17}$$

Solving for k and simplifying (taking the minimum of the quadratic solutions), the expression becomes:

$$k = \frac{EI - \sqrt{(EI)^2 - \frac{1}{2}\pi EI d_c h h_c^2 P_i\left(\frac{1}{2}\right)}}{EI h_c}. \tag{5.18}$$

From combining and simplifying eqs. (5.6), (5.7) and (5.18),

$$\theta = x_i k_i \tag{5.19}$$

$$\theta = \frac{x\left(EI - \sqrt{(EI)^2 - \frac{1}{2}\pi EId_c hh_c^2 P_i}\right)}{h_c\sqrt{(EI)^2 - \frac{1}{2}\pi EId_c hh_c^2 P_i}} \tag{5.20}$$

With the assumption that bending is uniform, the final expression for the bending angle of the entire structure as a function of pressure is as follows:

$$N\theta = \frac{Nx\left(EI - \sqrt{(EI)^2 - \frac{1}{2}\pi EId_c hh_c^2 P_i}\right)}{h_c\sqrt{(EI)^2 - \frac{1}{2}\pi EId_c hh_c^2 P_i}} \tag{5.21}$$

where:

- N is the number of chambers.

This analytical model is used for all iterations of the design to verify the first loading case results from Ansys before simulating the remaining LC.

5.3. Results

For a purely pressurised system with no external loading (LC1.1), the bending angle and pressure relationship had a strong alignment in results. The deviations in the Ansys model from the trend are due to the curvature of the end surface of the chamber. The angle is calculated as the average angle of the end surface to the YZ plane. However, as it inflates it also becomes elliptical, meaning the resultant angle is slightly skewed. Despite this, there is a strong agreement between the models (with a mean absolute error of 8.75°) verifying the accuracy of the results from Ansys for the remaining configurations.

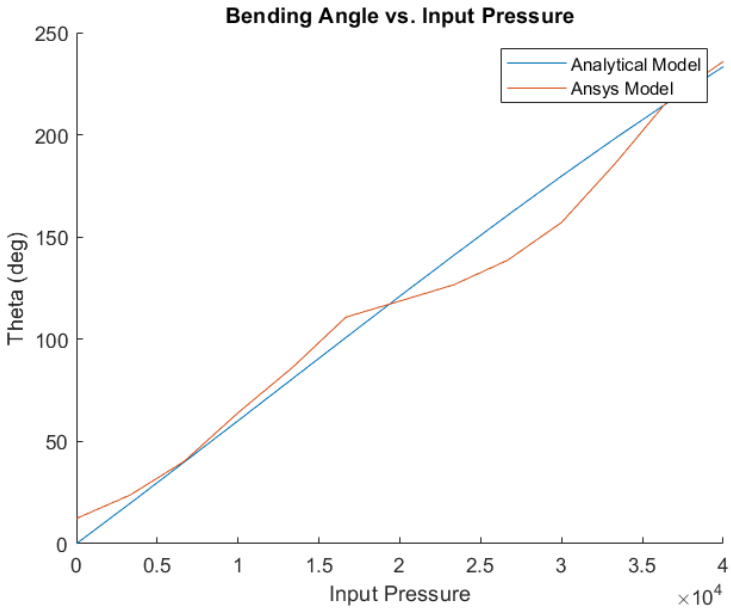

Figure 5.7: Comparison of bending angle as a function of internal pressure for the initial design. Modelled for LC1.1 comparing the analytical and Ansys results

This led to the remaining LCs being simulated to highlight any structural weaknesses in the proposed design.

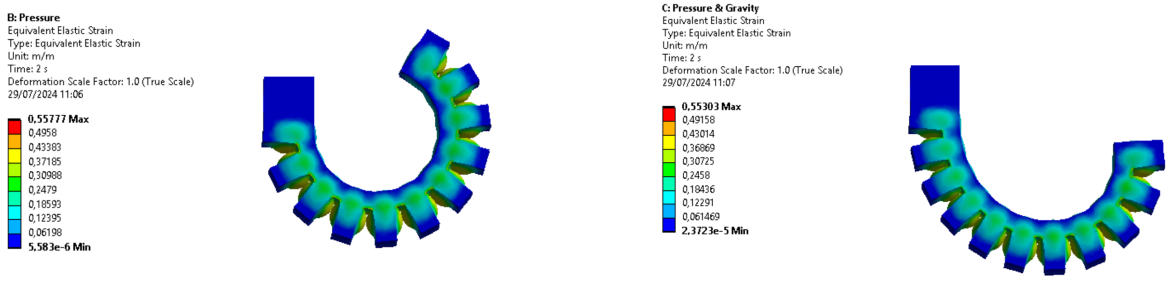

(a) Strain distribution under LC1.1

(b) Strain distribution under LC1.2

Figure 5.8: Uniform strain distribution under LC1.1 and LC1.2

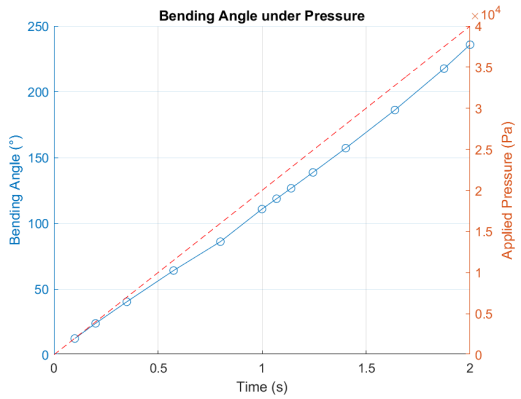

(a) Bending angle under pressure (LC1.1)

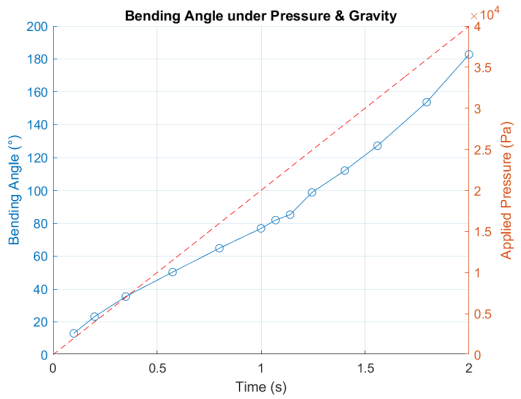

(b) Bending angle under pressure and gravity (LC1.2)

Figure 5.9: Bending angle over simulation time as a function of pressure in Ansys for LC1.1 and 2

If we look at the remaining LCs, it was concluded that the design was inherently unstable and unable to hold its form. The most extreme case can be seen in figs. 5.10a and 5.10b for LC1.3. The lack of pressure means that the actuator's ability to withstand deformation is purely a geometric and material function. Following this, the asymmetrical design means that the strain-limiting layer is not in the loading axis, making it an infeasible design. In comparison, for LC1.4 and 1.5 in figs. 5.10c to 5.10f the design is at least able to support the robot's weight and end in a more stable equilibrium as loading is in the axis of the strain limiting layer. However, this equilibrium is far from a uniform curvature, which would reduce both the lifespan and ease of control in rugged terrain.

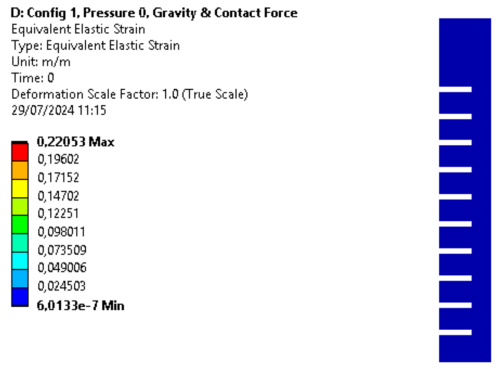

(a) Strain distribution at pre-LC1.3

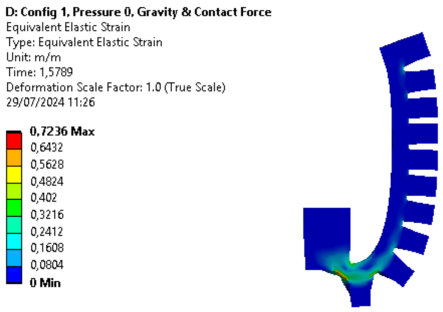

(b) Strain distribution at post-LC1.3

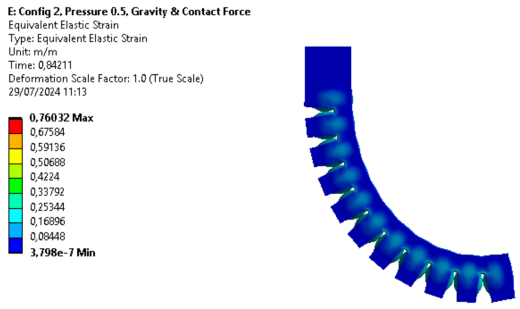

(c) Strain distribution at pre-LC1.4

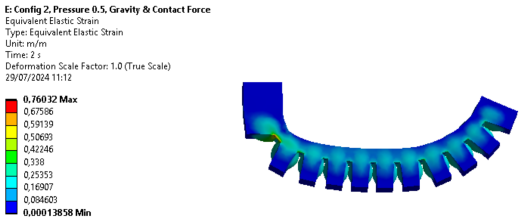

(d) Strain distribution at post-LC1.4

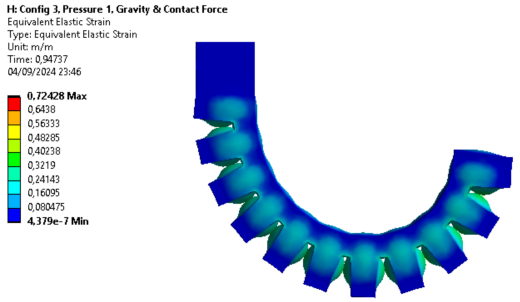

(e) Strain distribution at pre-LC1.5

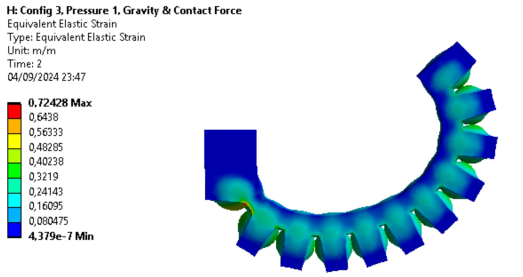

(f) Strain distribution at post-LC1.5

Figure 5.10: Strain distribution for LC1.3,4,5

The design's infeasibility is further confirmed by the large spikes in the bending angle, despite the loading being added gradually as seen in figs. 5.11a and 5.11b. The bending angle of LC1.3 was not computed, as the significant asymmetry and deformation meant that any data from this would be aimless.

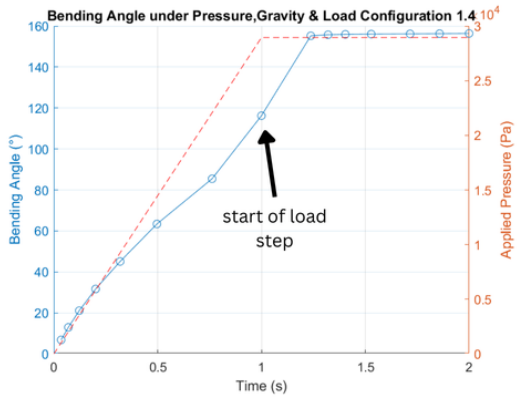

(a) Bending angle under pressure, gravity and LC1.4

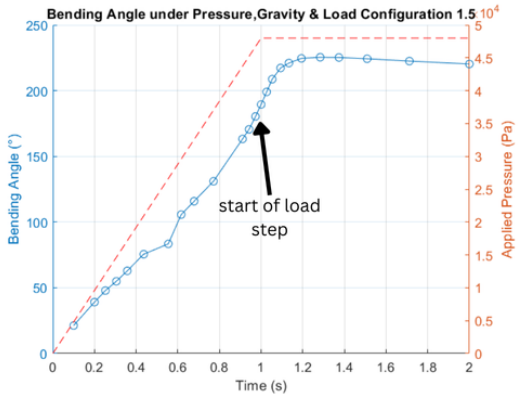

(b) Bending angle under pressure, gravity and LC1.5

Figure 5.11: Bending angle over simulation time as a function of pressure in Ansys for LC1.4,5

Looking at the stress, strain and overall deformation profile for all LCs (see Table 5.2), no material failure oc-

curred besides for LC1.3. The unstable structure resulted in the mechanism no longer becoming functional, a large element distortion and the solution not able to reach convergence beyond initial loading.

LC	Maximum Stress (kPa)	Maximum Strain
1.1	467	0.56
1.2	461	0.55
1.3	Non-Convergance	Non-Convergance
1.4	801	0.76
1.5	853	0.72

Table 5.2: Load cases with maximum stress and strain values for the initial design

From here, the main weaknesses of the first design are as follows. The neutral position cannot hold its self weight. The current design cannot utilise pressure to combat this, as any pressurisation would mean it's no longer at its neutral position. Hence, the strength of the structure at any other position is purely a function of the strain-limiting layer, but thickening this layer would only increase the operating pressure, making the system require more power. Instead, after multiple iterations of the design cycle, the following changes were made to obtain the final design as seen in Figure 5.12. The neutral position was changed to be the point of maximum curvature instead of straight. This meant that the structure could not deform past a point and remain stable. To further aid this, the chambers were brought closer together and were changed from rectangular to trapezoidal to make use of the stability of a triangular surface. This increases the surface area and therefore reduces the stresses throughout the structure. The depth of the outer chamber was increased such that the pressure would result in more of an uniaxial deformation to minimise twisting and distortion. Finally, the number of chambers was reduced as the change in curvature no longer required to be as large. With the new design, the maximum operating pressure drops as the structure doesn't need to curve as far to go from fully bent to up straight.

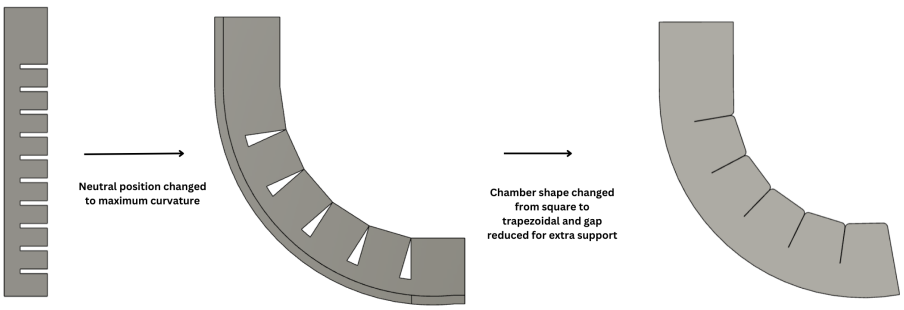

Figure 5.12: Changes made to achieve final design

The new and final design was again verified using the analytical model and the LCs seen in Table 5.3. An additional case (LC2.4) was added to see the maximum blocked force produced by the actuator where the point of contact with the ground is fixed as well, and a force reaction probe was added to determine the output produced at that boundary condition as seen in Figure 5.13.

Key	Value
Neutral	0 kPa
Inflated	0 - 50kPa
Fixed Support	0 DoF
External Load	1.25N

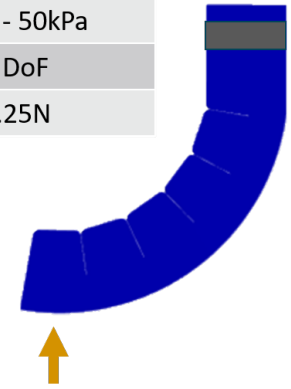

(a) LC2.3 - 0 Pressure Load Test

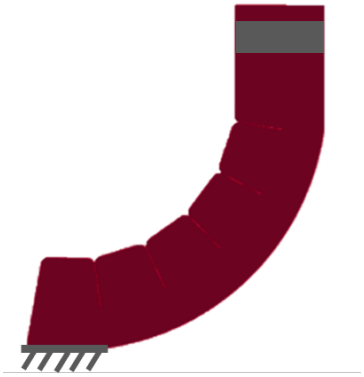

(b) LC2.4 - Blocked Force Test

Figure 5.13: Loading configurations performed to ensure structural feasibility

LC	Applied Pressure (kPa)	Gravitational Acceleration (m/s^2)	Contact Force (N)
2.1	30	0	0
2.2	30	-9.81	0
2.3	0	-9.81	1.25
2.4	50	-9.81	NA

Table 5.3: Input values for all LC's for the final design

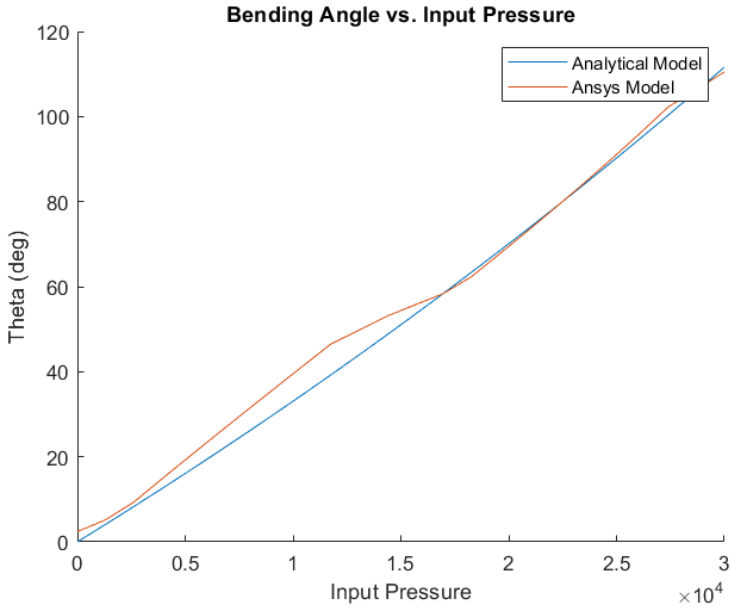

Figure 5.14: Comparison of bending angle as a function of internal pressure for the final design. Modelled for LC2.1 comparing the analytical and Ansys results

Again the analytical model proved to have strong agreement with the simulation results (with a mean absolute error of 2.51°, see Figure 5.14) with the design changes only being geometric. The following LCs were then simulated to obtain the final results.

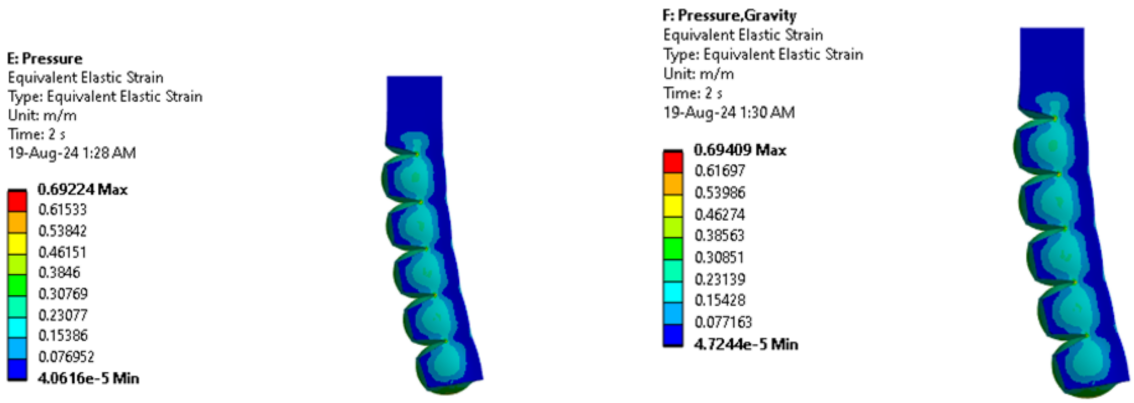

(a) Strain distribution under LC2.1 at maximum pressure

(b) Strain distribution under LC2.2 at maximum pressure

Figure 5.15: Uniform strain distribution under LC2.1 and LC2.2

From the strain results (see Figure 5.16) it is seen that pressure is distributed uniformly and that no material failure occurs (see Table 5.4). Its relationship of bending angle with pressure remained consistent even with the addition of gravity maintaining stable deformation when comparing figs. 5.16a and 5.16b and visually in figs. 5.15a and 5.15b with only a slight non-linearity being introduced when the pressure increased beyond 15kPa. The addition of external loading (LC2.3, 2.4) was then added to see the stability under self-weight as well as how much force it can generate when pressurised.

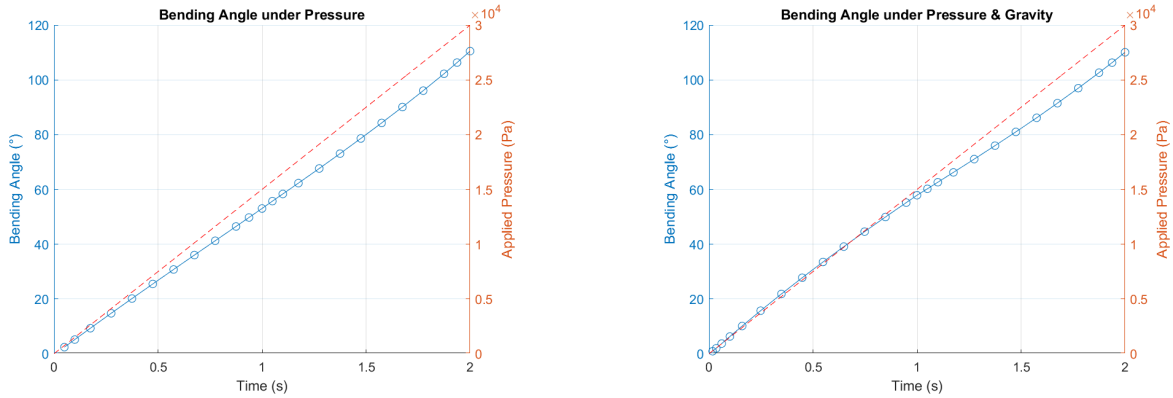

(a) Bending angle under pressure (LC2.1)

(b) Bending angle under pressure and gravity (LC2.2)

Figure 5.16: Bending angle over simulation time as a function of pressure in Ansys for LC2.1 and 2

The trapezoidal design provided significantly more stability to the wheel when under its self-weight (and no pressure) with the change in bending angle being negligible (as seen in Figure 5.17b). In comparison to the initial design, it is also more adaptable to changes in loading as the pressure can then be increased to keep the chambers bulging in the loading axis and not outwards, minimising the risk of failure due to twisting.

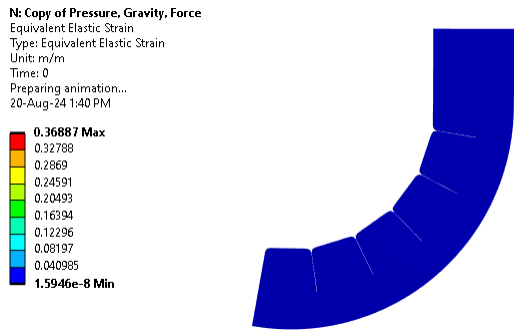

(a) Strain distribution at pre-LC2.3

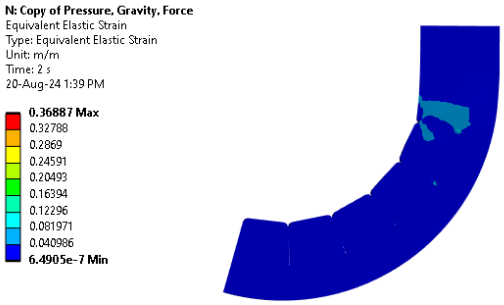

(b) Strain distribution at post-LC2.3

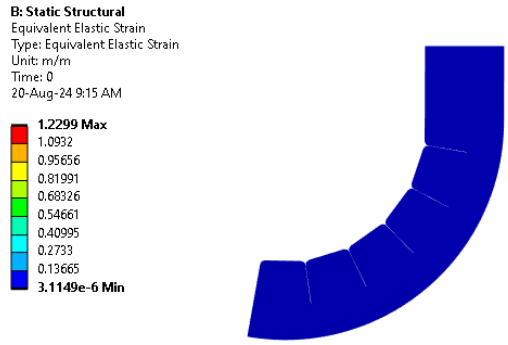

(c) Strain distribution at pre-LC2.4

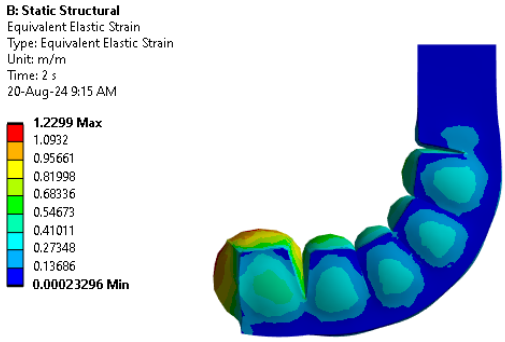

(d) Strain distribution at post-LC2.4

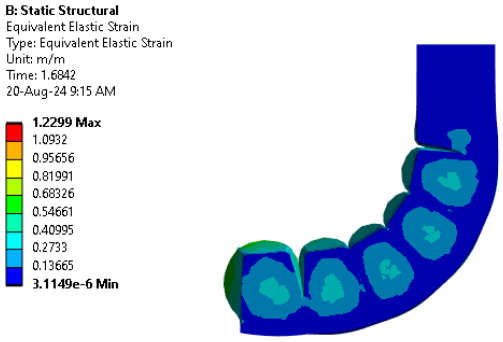

(e) Strain distribution at maximum operating point (LC2.4)

Figure 5.17: Strain distribution for LC2.3 and LC2.4

With its stability at a neutral state confirmed, the blocked force test examined how much force the structure could exert (and therefore lift) before material or operational failure. Blocked force is defined as the maximum force that can be applied by the system when generating zero displacement. From Figure 5.18, it can be seen that at peak pressures of 50kPa, it produced 3N. However, when analysing the strain values at that point (Figure 5.17d), although the system didn't experience material failure (see Table 5.4) the distribution became significantly non-uniform and wouldn't provide stable operation. Hence, from analysis, the operating blocked force was 1.98N (at 35kPa) as that was the point where all chambers were still a uniform volume maintaining the curvature of the limb as seen in Figure 5.17e.

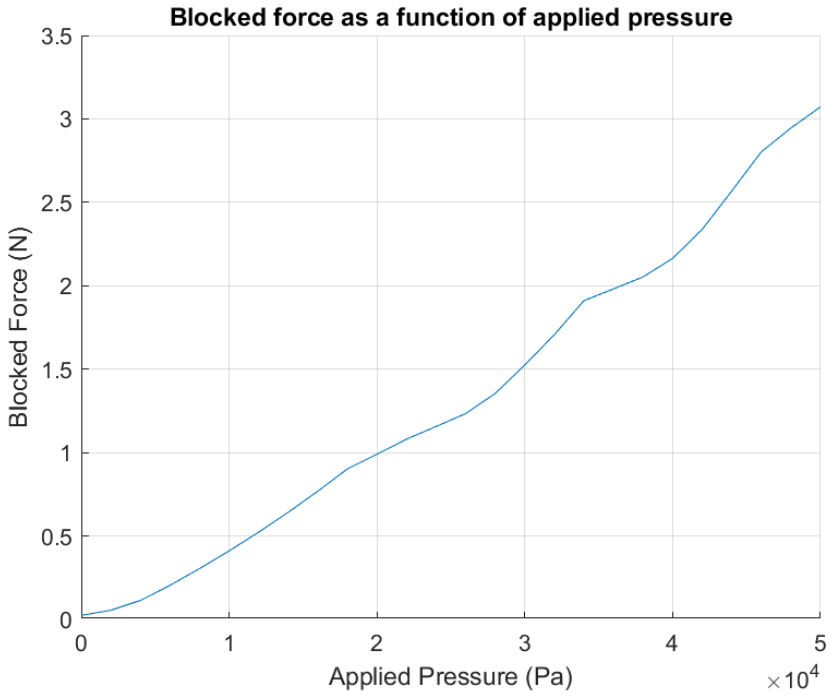

Figure 5.18: Blocked force as a function of pressure until operational failure

LC	Maximum Stress (kPa)	Maximum Strain
2.1	449	0.69
2.2	451	0.69
2.3	848	0.37
2.4	878	1.23

Table 5.4: Load cases with maximum stress and strain values for the final design

Overall, through the use of Ansys and verification of an analytical model, a final feasible design for the adaptable wheel was obtained. The changes made from the initial design meant that loading was in the axis of the strain-limiting layer making it more stable (even at 0kPa) and that pressure could be used to control to not only adjust the height of the wheel but withstand higher loads. The diameter of the wheel ranges from 230mm to 280mm depending on inflation.

6| Deformable Terrain Testing

6.1. Methodology

DEM coupled with multi-body dynamics (MotionSolve) was used to test the resultant design in deformable terrain. As per the requirements set in section 1.1, terrains of varying moisture and compressibility are tested to determine the versatility of the design. This particle characterisation was achieved by using the built-in terrain material database from EDEM Altair was used. All terrain materials had a Poisson's ratio, density and shear modulus of 0.25, 2.6 kg/m^3 and 10 MPa respectively. The coefficient of restitution was varied linearly between 0.48 and 0.36 from non-compressible dry, non-compressible sticky, compressible dry and compressible sticky respectively. The remaining values of static friction, rolling friction and surface energy can be seen in Table 6.2. To capture the cohesion, varying contact models including the Johnson-Kendall-Roberts(JKR) [21], Edinburgh-Elasto-Plastic-Adhesive (EEPA) [43] and Hysteretic Spring (HS) [49] contact model was used. The interaction properties between the robot and terrain were obtained from a tyre and sandy soil literature study, as reliable values calibrated for discrete element simulations for Dragon Skin 30 were not available [20]. The robot material properties were obtained from standard silicone rubber and can be seen in Table 6.1.

Parameter	Value
Sliding Friction (μ_s)	0.55
Rolling Friction (μ_r)	0.37
Density (ρ)	1100 kg/m^3
Poisson's Ratio (ν)	0.33
Elastic Modulus (E)	0.05 GPa

Table 6.1: Robot Material and Interaction Properties

Terrain Material behaviour	Co. of Restitution	Co. of Static Friction	Co. of Rolling Friction	Surface Energy (J/m^2)
Non-compressible Dry	0.55	0.2	0.1	0 (JKR)
Compressible Dry	0.35	0.2	0.05	0 (HS)
Non-compressible Sticky	0.55	0.2	0.1	3.75 (JKR)
Compressible Sticky	0.55	0.2	0.1	50 (EEPA)

Table 6.2: Material Properties for each EDEM Simulation [2]

Due to the high computation required in generating a large number of particles as well as coupling with another software, the terrain is limited to a size of 3 x 4 x 0.8m. In terms of the robot's dynamics, the wheel can only be simulated as a rigid body. Due to this, 3 key operating configurations were chosen and exported in their deformed state from Ansys to a mesh. This single limb mesh was then converted back into a full wheel to be used in the simulation as seen in Figure 6.1.

(a) Neutral state **(b)** Partially inflated state **(c)** Fully inflated state

Figure 6.1: Wheel operating configurations simulated in a deformable terrain

For each simulation, the terrain volume was filled using a static factory (averaging between 30,000-35,000 particles)of each material and allowed to settle before the coupling with the multi-body dynamics software. The aim was to see how far different wheel configurations would travel across different terrains in 5 seconds, the ride height, and if the design proved beneficial in certain configurations over others. Hence, each joint was given a constant velocity of $2\pi rad/s$. Once set up, MotionSolve would create an instance of the robot, dropping it into the EDEM terrain before applying the forward velocity as seen in Figure 6.2d. This was repeated for each wheel configuration in the EDEM terrain with the displacement measured as seen in Figure 6.2. With 4 sand types and 3 wheel configurations, a total of 12 simulations were run.

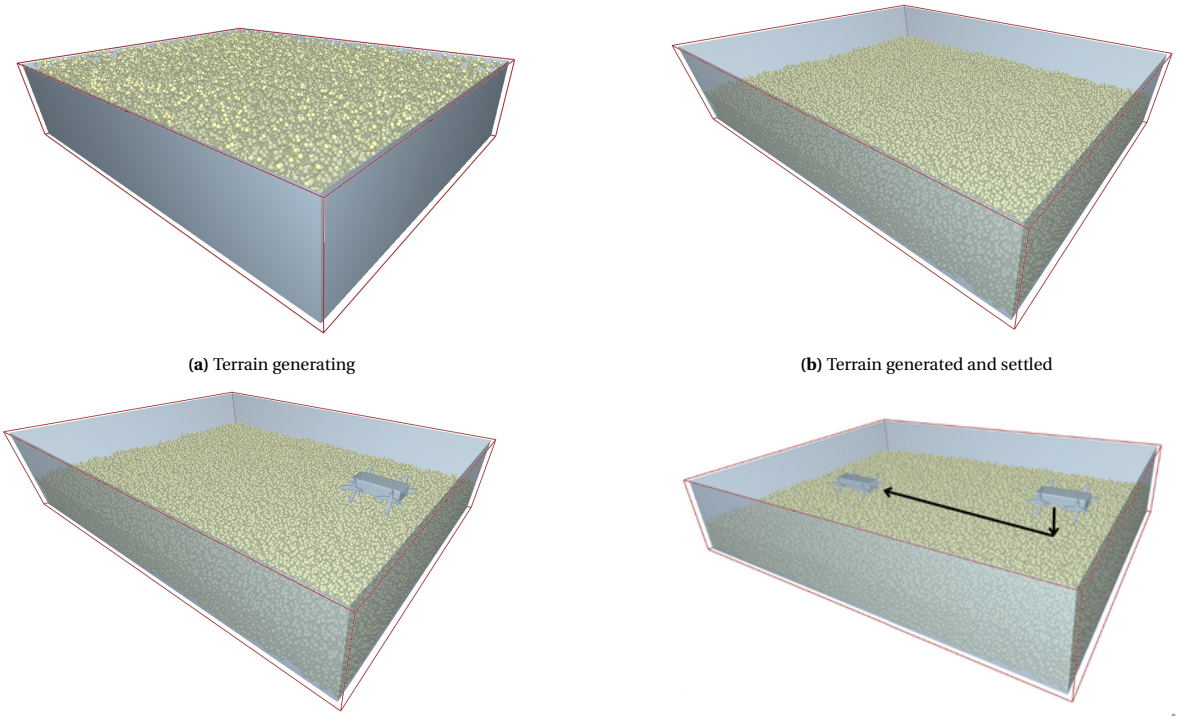

(a) Terrain generating

(b) Terrain generated and settled

(c) Terrain coupled with multi-body dynamics of the robot

(d) Path taken by robot during simulation

Figure 6.2: Schematic for the simulation setup for deformable terrain testing

6.2. Results

The conclusions of the result were obtained from both the quantitative data alongside the visual simulation to better understand the trends. The first key result is the average height of the robot over the simulation timeframe for all sand types in Figure 6.3. The overall oscillating nature of all wheels is due to the gaps between the limbs on each wheel, temporarily lowering the structure supporting the robot. However, the amplitude range as well as the overall average height indicates how much the wheels sink into the deformable terrain. The conclusions of this (see Figure 6.3) are as follows. Despite having the smallest diameter, the neutral design has the highest average (i.e. sinks the least) of the 3 wheel configurations. This is due to it having the largest contact area with the ground. The amplitude range during the simulation shows that the fully inflated design lifts the robot the most off the ground as expected, but likewise sinks and drops significantly with each rotation. This is due to the smaller contact area it has with the ground in comparison with the other designs. Interestingly, the partially inflated wheel sinks the most into the terrain, with the curved contact surface digging the wheel into the particles.

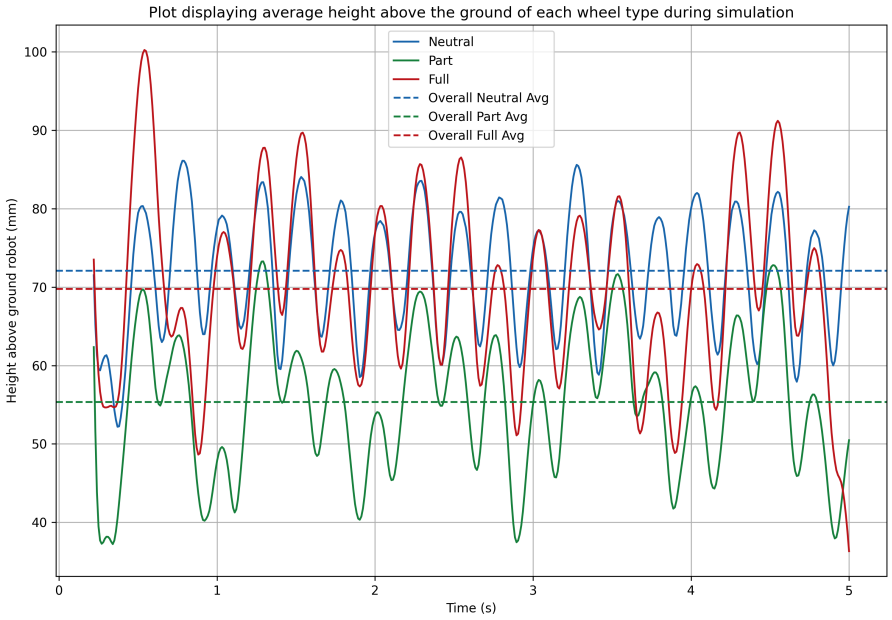

Figure 6.3: Average height during simulation above the ground for each wheel configuration across all sand types

A higher wheel height on one hand reduces the friction that needs to be overcome to move across the surface, but likewise reduces the friction available to create the required forward tangential force. The designs also vary in diameter, with a larger diameter travelling further per rotation than a smaller wheel. This is immediately clear in Figure 6.4 as the fully inflated design travels the furthest in each terrain (average of 3.4m versus 2.9m and 2.6m for the other configurations). However, interestingly, the higher ride height of the neutral design (higher by 15mm on average) outweighs the larger diameter of the partially inflated design, travelling the second furthest in all terrains. Despite there being no terrain-dependent results in terms of distance covered, the height above the ground is terrain-dependent as seen in Figure 6.5. The neutral configuration performed best on compressible sticky and non-compressible dry with the opposite being true for the fully inflated option.

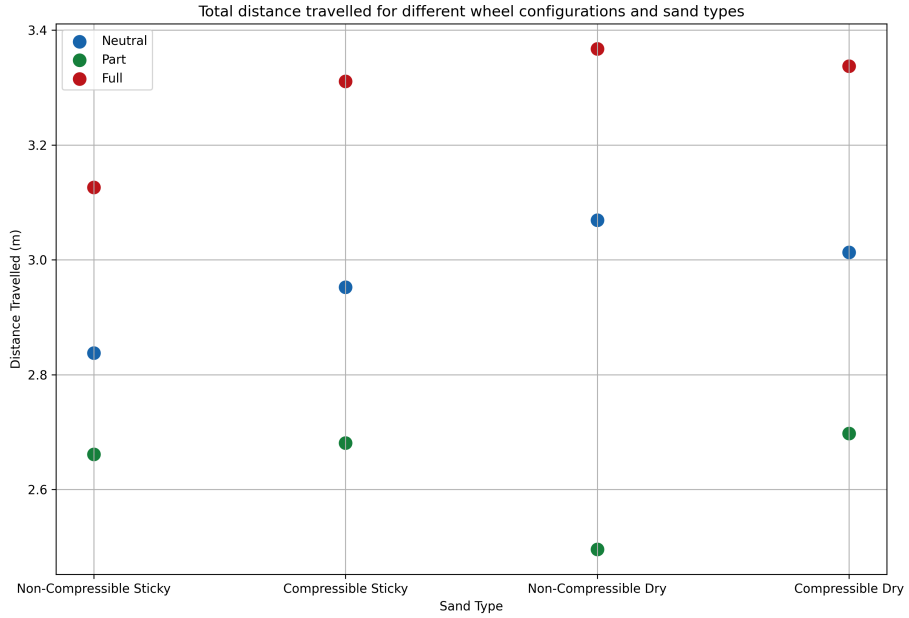

Figure 6.4: Total distance travelled by each wheel configuration across all sand types

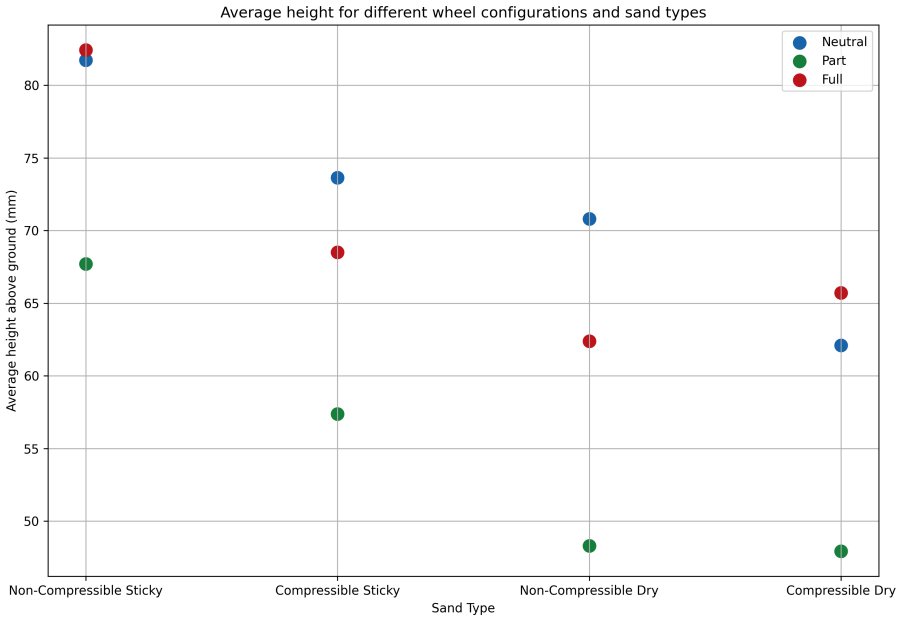

Figure 6.5: Average height above the ground for each wheel configuration across all sand types

Overall, the simulations showed having an adaptable system to be beneficial in traversing varying terrains. Both wheel geometry, contact area and moisture level all affected the performance of the wheel. The wheel is the least efficient when transitioning between the extreme configurations (at partially inflated) which can inform the decision-making if designing a control strategy. For full applications, the adaptability in performance characteristics can be beneficial to make a robot more multi-functional. For example, if power consumption is key, the neutral design can be used, requiring no power to go to inflation of the wheel. Likewise, if reduced sinkage into the ground is needed (e.g. in agriculture where the topsoil is delicate) the form can be changed accordingly. It proved the most stable and still suitable for a variety of terrains per figs. 6.3 and 6.4. Likewise, if there are large terrain variations (from tidal patterns) or obstacles, the wheel's geometry can be adjusted accordingly.

7| Discussion

7.1. Design Framework

The framework (outlined in the design cycle Figure 2.1) used to get to the resultant design both improved the model and tested it in its intended environment. Starting from the initial form of a cyclic paddler due to its kinematic advantages over other forms of locomotion, the effect of varying design choices (number and shape of limbs) was tested in varying rugged terrains. This allowed an analysis of how successful a certain design was in overcoming different obstacles that may be present in the environment. From here, the key performance indicators were considered to select a single design moving forward with the introduction of the soft material properties. Although its high-strain compliance is a key advantage of the design, it had to be ensured that this flexibility was still structurally stable enough to withstand the operational loads. Finally, the optimised design was tested in varying deformable terrains to test not only its efficiency but also if its adaptability in form had any advantage in travelling across different environments. A summary of the design framework can be seen in Figure 7.1.

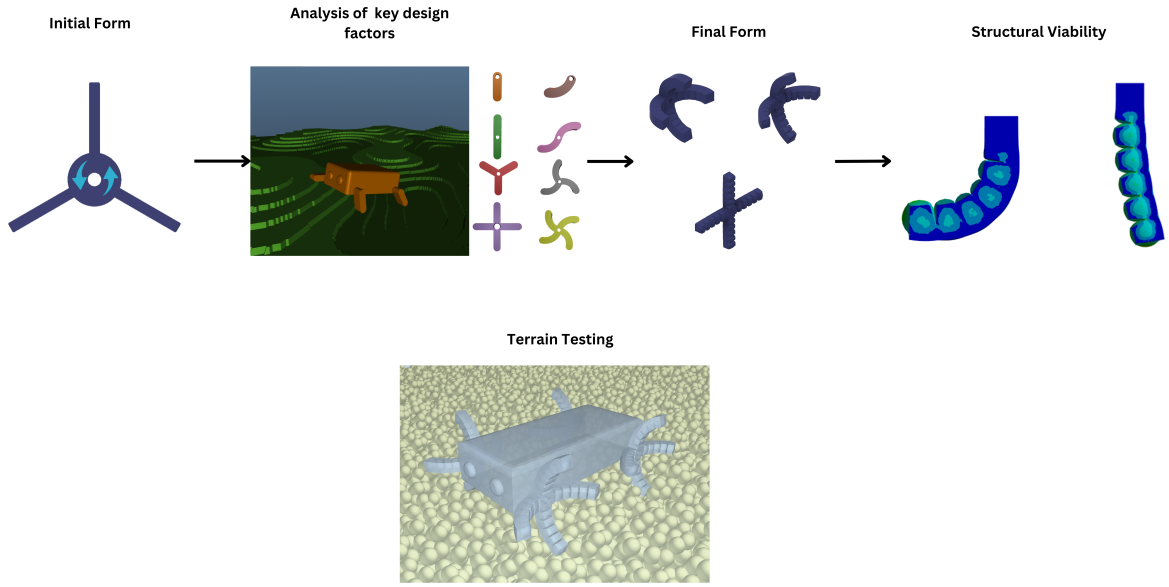

Figure 7.1: Summary of the framework used in the design proces

7.2. Conclusion

The 3 design loops in the project led to a final feasible model for a novel adaptable soft wheel. The kinematic analysis showed that a higher number of limbs on the wheel increased its suitability to more terrains, however, there was no clear discernable difference between 3 or 4 limbs. It also highlighted the necessity for an adaptable design, with the shape of the limb as well as the robot's ability to upright itself being more important than initial stability or speed. The isolation of each limb's pneumatic chambers aids the individual actuation for more complex terrains. The resultant design had an operating pressure of 0-30kPa and was able to support a load of 1.25N in compression, making it suitable for a robot of 500g (given 4 wheels). It had an absolute maximum blocked force of 3N, but this proved operationally unstable with non-uniform strain. The operational limit was found to be 1.98N at 35kPa. Finally, the model was tested in 4 different sand types at 3 different operating modes. The fully inflated wheel travelled the furthest due to its larger diameter, however did have the largest oscillations and a lower overall ride height in comparison to the neutral wheel. The wheel when transitioning between states was the least efficient as it was the most submerged in the terrain.

7.3. Future Work & Potential Applications

This proposed design is aimed to be a starting point to increase the reach of robotic systems in environmental applications in a non-hazardous or damaging matter. Future work for this project would include manufacturing various prototypes to further validate the concept and test it outside laboratory settings to determine its lifespan (e.g. cycles till fatigue failure). A second key area of research would be creating the necessary control strategy to aid the smooth operation of the robot. This control strategy would be both

for the entire form of the wheel and more interestingly explore individual actuation of each limb to create a more compliant system. The current design was aimed at a 500g robot, however, due to its simplicity and symmetry, it can be easily scaled according to the application at hand. It would be interesting to explore the use of composite options or the jamming effect with particles inside. Although needing 2 forms of actuation (A DC motor and a compressor), its stability at 0kPa means it is still stable and functional if power consumption needs to be conserved. Hence, further research into lighter and more efficient batteries, motors, and pumps will increase its capability in the intended environments.

Its adaptable design lends itself to applications in environments that are constantly changing. Its intended terrain means potential use in agricultural settings, exploration, biodiversity monitoring and even potential space applications as the design can compress for transport and inflated on-site. Its simplicity aids in creating other chassis designs beyond the simple 4-wheel option proposed in this project (see Figure 7.2d). A more detailed example would be a mangrove environment which is heavily rooted and is constantly changing in moisture due to tides but difficult to get to. Such a system has the potential to have individually actuating limbs that can expand when needing to climb the roots while collapsing when having to squeeze through gaps. Likewise, it would be interesting to develop this idea further for amphibious terrains, with the wheel form having the potential to be utilised in a propeller setting. Examples of potential use cases can be seen in Figure 7.2. Future research efforts are needed to test the design; however, with the simplicity of the base locomotion (a rotating wheel), the expectation is that it can achieve higher technology readiness levels more quickly, thanks to its compatibility with off-the-shelf components.

(a) A seed hopper for reforestation projects

(b) Biodiversity monitoring

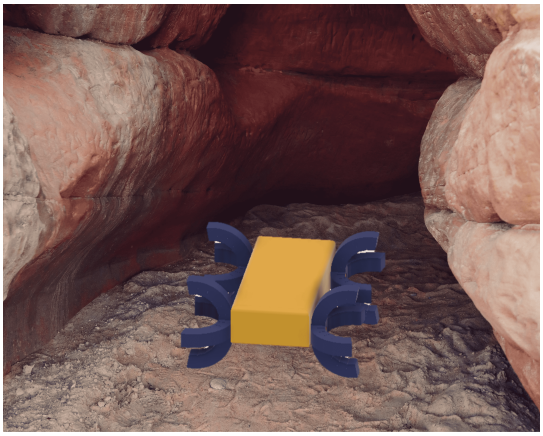

(c) Lower ride height requirement for cave exploration

(d) Amphibious potential for water quality measurement

Figure 7.2: Schematic for example use cases of the adaptive wheel concept

References

[1] Gunjan Agarwal, Nicolas Besuchet, Basile Audergon, and Jamie Paik. Stretchable materials for robust soft actuators towards assistive wearable devices. Scientific reports, 6(1):34224, 2016.

[2] Altair Engineering Inc. Soils starter pack, 2022. [Accessed: August 11, 2024].

[3] Travis Archer. Procedurally generating terrain. In 44th annual midwest instruction and computing symposium, Duluth, pages 378–393, 2011.

[4] Howard A Barnes, John Fletcher Hutton, and Kenneth Walters. An introduction to rheology, volume 3. Elsevier, 1989.

[5] A. S. Boxerbaum, R. J. Bachmann, R. D. Quinn, R. M. Harkins, T. Dunbar, S. C. Burgess, and R. Vaidyanathan. Design and testing of a highly mobile insect-inspired autonomous robot in a beach environment. International Journal of Design and Nature and Ecodynamics, 4, 2009.

[6] Pinar Boyraz, Gundula Runge, and Annika Raatz. An overview of novel actuators for soft robotics. actuators, 7, 6 2018.

[7] Guizhou Cao, Bing Chu, and Yanhong Liu. Analytical modeling and control of soft fast pneumatic networks actuators. In IECON 2020 The 46th annual conference of the IEEE industrial electronics society, pages 2760–2765. IEEE, 2020.

[8] Terry Ching, Joseph Zhi Wei Lee, Shane Kyi Hla Win, Luke Soe Thura Win, Danial Sufiyan, Charlotte Pei Xuan Lim, Nidhi Nagaraju, Yi-Chin Toh, Shaohui Foong, and Michinao Hashimoto. Crawling, climbing, perching, and flying by fiba soft robots. Science Robotics, 9(92):eadk4533, 2024.

[9] Asaf Dana, Shahaf Vollach, and Doron Shilo. Use the force: review of high-rate actuation of shape memory alloys, 2021.

[10] Viljoen Du Toit. Characterising material models for silicone-rubber using an inverse finite element model updating method. PhD thesis, Stellenbosch: Stellenbosch University, 2018.

[11] Nazek El-Atab, Rishabh B Mishra, Fhad Al-Modaf, Lana Joharji, Aljohara A Alsharif, Haneen Alamoudi, Marlon Diaz, Nadeem Qaiser, and Muhammad Mustafa Hussain. Soft actuators for soft robotic applications: A review. Advanced Intelligent Systems, 2(10):2000128, 2020.

[12] Steven Floyd and Metin Sitti. Design and development of the lifting and propulsion mechanism for a biologically inspired water runner robot. IEEE Transactions on Robotics, 24, 2008.

[13] M. Follador, M. Cianchetti, A. Arienti, and C. Laschi. A general method for the design and fabrication of shape memory alloy active spring actuators. Smart Materials and Structures, 21, 11 2012.

[14] Zahra Sadat Navabi Ghamsari. The introduction and analysis of a novel soft actuator for a soft continuum robot arm. Master's thesis, University of Minnesota, 2018.

[15] Roza Gkliva and Maarja Kruusmaa. Soft fluidic actuator for locomotion in multi-phase environments. IEEE Robotics and Automation Letters, 7, 2022.

[16] Simon Godon, Maarja Kruusmaa, and Asko Ristolainen. Maneuvering on non-newtonian fluidic terrain: a survey of animal and bio-inspired robot locomotion techniques on soft yielding grounds, 2023.

[17] Carlo Greco, Parth Kotak, Leonardo Pagnotta, and Caterina Lamuta. The evolution of mechanical actuation: from conventional actuators to artificial muscles, 2022.

[18] A Gulliver, PE Carnell, SM Trevathan-Tackett, MD de Paula Costa, P Masqué, and PI Macreadie. Estimating the potential blue carbon gains from tidal marsh rehabilitation: a case study from south eastern australia. frontiers in marine science 7: 403, 2020.

[19] Jonathan Hiller and Hod Lipson. Dynamic simulation of soft multimaterial 3d-printed objects. Soft robotics, 1(1):88–101, 2014.

[20] Cheng Hu, Jingwei Gao, Jincheng Diao, and Xiaobo Song. Numerical simulation of tire steering on sandy soil based on discrete element method. AIP Advances, 11(1), 2021.

[21] Kenneth Langstreth Johnson, Kevin Kendall, and AAD Roberts. Surface energy and the contact of elastic solids. Proceedings of the royal society of London. A. mathematical and physical sciences, 324(1558):301–313, 1971.

[22] Xiang juan Bai, Jian zhong Shang, Zi rong Luo, Tao Jiang, and Qian Yin. Development of amphibious biomimetic robots. Journal of Zhejiang University-SCIENCE A 2022 23:3, 23:157–187, 3 2022.

[23] Mohammad Mahdi Kheirikhah, Samaneh Rabiee, and Mohammad Ehsan Edalat. A review of shape memory alloy actuators in robotics. volume 6556 LNAI, 2011.

[24] Hyung Jung Kim, Sung Hyuk Song, and Sung Hoon Ahn. A turtle-like swimming robot using a smart soft composite (ssc) structure. Smart Materials and Structures, 22, 2013.

[25] Matthew A. Klein, Alexander S. Boxerbaum, Roger D. Quinn, Richard Harkins, and Ravi Vaidyanathan. Seadog: A rugged mobile robot for surf-zone applications. 2012.

[26] Andrew D. Marchese, Robert K. Katzschmann, and Daniela Rus. A recipe for soft fluidic elastomer robots. Soft Robotics, 2, 2015.

[27] Andrew D Marchese, Robert K Katzschmann, and Daniela Rus. A recipe for soft fluidic elastomer robots. Soft robotics, 2(1):7–25, 2015.

[28] Andrew D. Marchese, Cagdas D. Onal, and Daniela Rus. Autonomous soft robotic fish capable of escape maneuvers using fluidic elastomer actuators. Soft Robotics, 1:1–101, 3 2014.

[29] Andrew D. Marchese and Daniela Rus. Design, kinematics, and control of a soft spatial fluidic elastomer manipulator. International Journal of Robotics Research, 35:840–869, 6 2016.

[30] Edoardo Milana, Bert Van Raemdonck, Kevin Cornelis, Enrique Dehaerne, Jef De Clerck, Yarno De Groof, Toon De Vil, Benjamin Gorissen, and Dominiek Reynaerts. Eelworm: A bioinspired multimodal amphibious soft robot. 2020.

[31] Seyed M. Mirvakili and Ian W. Hunter. Artificial muscles: Mechanisms, applications, and challenges, 2 2018.

[32] United Nations. Percentage of total population living in coastal areas. Technical report, United Nations, June 2007.

[33] Abhishek Manoj Patel. Design and analysis of soft actuator with enhanced stiffness with granular jamming. Master's thesis, University of Windsor (Canada), 2022.

[34] Elze Porte, Sophia Eristoff, Anjali Agrawala, and Rebecca Kramer-Bottiglio. Characterization of temperature and humidity dependence in soft elastomer behavior. Soft Robotics, 11(1):118–130, 2024.

[35] Daniela Rus and Michael T. Tolley. Design, fabrication and control of soft robot using fluidic elastomer actuators. Nature, 521, 2015.

[36] Robert F Shepherd, Filip Ilievski, Wonjae Choi, Stephen A Morin, Adam A Stokes, Aaron D Mazzeo, Xin Chen, Michael Wang, and George M Whitesides. Multigait soft robot. Proceedings of the national academy of sciences, 108(51):20400–20403, 2011.

[37] Langquan Shui, Liangliang Zhu, Zhe Yang, Yilun Liu, and Xi Chen. Energy efficiency of mobile soft robots. Soft Matter, 13(44):8223–8233, 2017.

[38] Inc. Smooth-On. Dragon skin 30 product information, 2024. Accessed: 2024-07-29.

[39] K Soman. International system of units: A handbook on SI unit for scientists and engineers. PHI Learning Pvt. Ltd., 2010.

[40] M. Sreekumar, T. Nagarajan, M. Singaperumal, M. Zoppi, and R. Molfino. Critical review of current trends in shape memory alloy actuators for intelligent robots. Industrial Robot, 34, 2007.

[41] Charbel Tawk and Gursel Alici. Finite element modeling in the design process of 3d printed pneumatic soft actuators and sensors. Robotics, 9(3):52, 2020.

[42] DeepMind Technologies. Mujoco documentation, 2024. Accessed: 2024-07-10.

[43] Subhash C Thakur, John P Morrissey, Jin Sun, JF Chen, and Jin Y Ooi. Micromechanical analysis of cohesive granular materials using the discrete element method with an adhesive elasto-plastic contact model. Granular Matter, 16:383–400, 2014.

[44] Michael T. Tolley, Robert F. Shepherd, Bobak Mosadegh, Kevin C. Galloway, Michael Wehner, Michael Karpelson, Robert J. Wood, and George M. Whitesides. A resilient, untethered soft robot. Soft Robotics, 1:213–223, 9 2014.

[45] Michael T Tolley, Robert F Shepherd, Bobak Mosadegh, Kevin C Galloway, Michael Wehner, Michael Karpelson, Robert J Wood, and George M Whitesides. A resilient, untethered soft robot. Soft robotics, 1(3):213–223, 2014.

[46] Barry Trimmer. Soft robots and society, 3 2015.

[47] Deepak Trivedi, Christopher D Rahn, William M Kier, and Ian D Walker. Soft robotics: Biological inspiration, state of the art, and future research. Applied bionics and biomechanics, 5(3):99–117, 2008.

[48] Annemiek Van Boeijen, Jaap Daalhuizen, Roos Van Der Schoor, and Jelle Zijlstra. Delft design guide: Design strategies and methods. 2014.

[49] Otis R Walton and Robert L Braun. Viscosity, granular-temperature, and stress calculations for shearing assemblies of inelastic, frictional disks. Journal of rheology, 30(5):949–980, 1986.

[50] Tsun-Hsuan Wang, Pingchuan Ma, Andrew Everett Spielberg, Zhou Xian, Hao Zhang, Joshua B Tenenbaum, Daniela Rus, and Chuang Gan. Softzoo: A soft robot co-design benchmark for locomotion in diverse environments. arXiv preprint arXiv:2303.09555, 2023.

[51] Zhenlong Wang, Guanrong Hang, Jian Li, Yangwei Wang, and Kai Xiao. A micro-robot fish with embedded sma wire actuated flexible biomimetic fin. Sensors and Actuators, A: Physical, 144, 2008.

[52] J.Y. Wong. Theory of Ground Vehicles. Wiley, 2008.

[53] Matheus S Xavier, Andrew J Fleming, and Yuen K Yong. Finite element modeling of soft fluidic actuators: Overview and recent developments. Advanced Intelligent Systems, 3(2):2000187, 2021.

[54] Fei Yang, Qi Ruan, Yiming Man, Zhijie Xie, Honghao Yue, Bing Li, and Rongqiang Liu. Design and optimize of a novel segmented soft pneumatic actuator. IEEE Access, 8:122304–122313, 2020.

[55] Yee Ling Yap, Swee Leong Sing, and Wai Yee Yeong. A review of 3d printing processes and materials for soft robotics. Rapid Prototyping Journal, 26(8):1345–1361, 2020.

[56] Tingnan Zhang, Feifei Qian, Chen Li, Pierangelo Masarati, Aaron M. Hoover, Paul Birkmeyer, Andrew Pullin, Ronald S. Fearing, and Daniel I. Goldman. Ground fluidization promotes rapid running of a lightweight robot. volume 32, 2013.

[57] Chuanqi Zheng, Siddharth Sane, Kangneoung Lee, Vishnu Kalyanram, and Kiju Lee. -waltr: Adaptive wheel-and-leg transformable robot for versatile multiterrain locomotion. IEEE Transactions on Robotics, 39:941–958, 4 2023.

[58] Jun Zhong, Minzhou Luo, Xiaofeng Liu, Jizhuang Fan, and Jie Zhao. Frog-inspired jumping robot actuated by pneumatic muscle actuators. Advances in Mechanical Engineering, 10, 6 2018.

[59] Öncay ; Yasa, Yasunori ; Toshimitsu, Mike Y ; Michelis, Lewis S ; Jones, Miriam ; Filippi, Thomas ; Buchner, and Robert K Katzschmann. An overview of soft robotics. 2023.

[60] Łukasz Fracczak, Michał Olejniczak, and Leszek Podsedkowski. Long-range snake-like robot powered by pneumatic mckibben muscles. Archive of Mechanical Engineering, 66:257–267, 2019.

8| Appendix

8.1. Perlin Noise Settings

$$\text{width} = 512 \tag{8.1}$$

$$\text{height} = 512 \tag{8.2}$$

$$\text{scale} = 100.0 \tag{8.3}$$

$$\text{octaves} = 1 \tag{8.4}$$

$$\text{persistence} = 0.3 \tag{8.5}$$

$$\text{lacunarity} = 0.5 \tag{8.6}$$

$$\text{seed} = 0 \tag{8.7}$$

8.2. MuJoCo Settings

$$\text{integrator} = \text{implicitfast} \tag{8.8}$$

$$\text{cone} = \text{elliptic} \tag{8.9}$$

MuJoCo uses unspecified units, meaning the user can use any units as long as they are consistent. For the simulations in this paper, SI units were utilised with MKS as the base [39].

8.3. Ansys Settings

The following settings were used in Ansys Mechanical to run the structural feasibility tests. Only the settings that are different to the default have been mentioned.

Mesh Settings

$$\text{Physics Preference} = \text{Nonlinear Mechanical} \tag{8.10}$$

$$\text{Capture Proximity Sizing} = \text{On} \tag{8.11}$$

Analysis Settings

$$\text{Large Deflection} = \text{On} \tag{8.12}$$

For load cases regarding pressure and gravity and no external loading:

$$\text{Number of Steps} = 1 \tag{8.13}$$

For load cases regarding pressure and gravity and external loading (to be added in the second step):

$$\text{Number of Steps} = 2 \tag{8.14}$$

$$\text{Minimum Subteps} = 10 \tag{8.15}$$

$$\text{Maximum Subteps} = 1000 \tag{8.16}$$

Actuation Method

To inflate the chambers, a linearly increasing pressure (up to the desired value) was added to all inner hollow walls of the chambers. This causes the structure to uniformly inflate however due to the strain-limiting layer, actuation will occur in 1 axis.

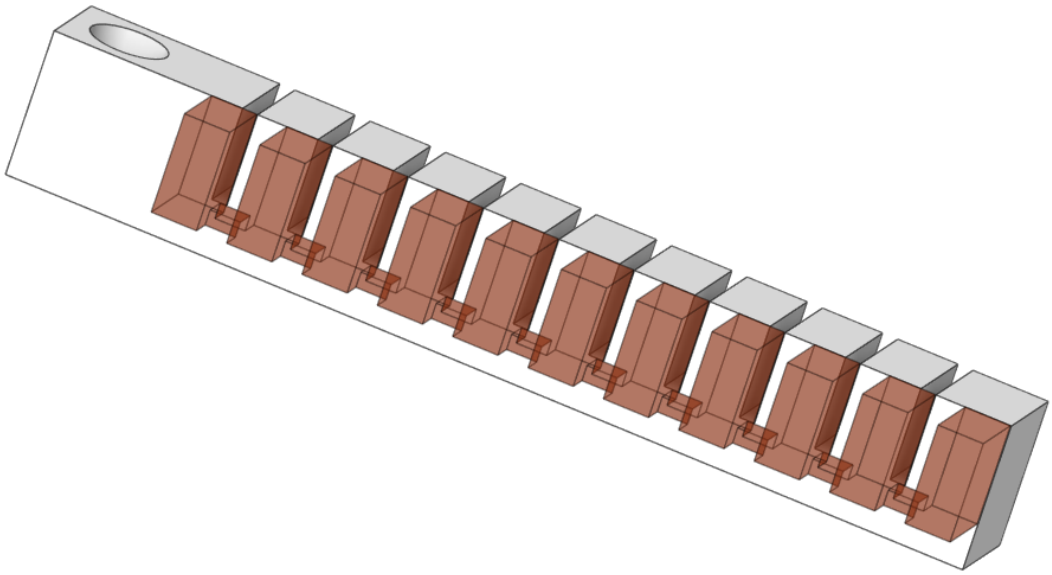

Figure 8.1: Schematic of inner walls

Modelling of a novel soft locomotive system for the exploration of rugged and deformable terrain

Gaetan Pans[1] and Dr. Jovana Jovanova[2]

***Abstract*— The importance of natural environments with rugged deformable terrain from biodiversity, carbon capture, and coastal protection to economic livelihood is significant. However, the current systems available for robots to explore those ecosystems are either large, expensive and intrusive, not application focused or consist of many mechanical parts prone to failure. This paper proposes a novel soft adaptable wheel suited for such ecosystems. Due to the significance of the material dynamics and their interactions with varying deformable terrain, modelling was employed in this paper as a robust tool, leveraging Finite Element Method (FEM) to efficiently capture the hyperelastic behaviours and the discrete element method (DEM) to capture the terrain dynamics, a process that would be time-consuming and resource-intensive if approached solely through experimental and construction methods. The mechanism operates as a soft fluidic actuator constructed with silicone, able to change its form depending on the task at hand. The design's structural feasibility was then tested and further analysed by FEM with the final result having a loading capacity of 1.25N (at 0kPa) and a maximum blocked force of 1.98N (at 35kPa). Finally, the wheel was tested at 3 distinct operating configurations of neutral, partial and fully inflated in 4 types of deformable terrain, including non-compressible dry, compressible dry, non-compressible sticky, and compressible sticky utilised DEM. The results evaluated the performance and validated the need for different wheel configurations according to the rheological properties of the terrain. In conclusion, the model proposed in this paper is intended to be more application-focused, with its simplicity facilitating integration into robotic systems, using off-the-shelf components, and ultimately reducing the time required to be used in environmental applications.**

Keywords

Soft Robotics, Deformable Terrain, Soft Fluidic Actuator, Adaptable, Locomotion

I. INTRODUCTION

Robotic systems capable of traversing rugged, deformable terrains (e.g., sand, soil, forests, marshes) remain scarce. Current commercial systems, like off-road vehicles, are large, expensive, and damaging to the environment. While smaller multi-terrain robots, such as SeaDog by Klein et al. [27], have been proposed, they are still rigid and lack the adaptability seen in nature. Though bio-mimetic designs have made strides, such as an eelworm-inspired robot with soft fluidic actuators [22], snake-like robots using McKibben actuators [23], frog-inspired jumping robots [24], and turtle-inspired designs with shape memory alloy wires embedded in polymer composites [26], they often remain tethered to labs due to high power requirements and complexity, limiting real-world application [21]. Tolley et al.'s multi-modal robot [25] is a notable exception, though it velocity is relatively slow and its unique design is difficult to incorporate into traditional robotic systems. This study proposes a solution that balances the flexibility of soft actuators, which mimic materials found in nature with elastic moduli in the range of 10^4 to 10^9 Pa [28], with the practicality of traditional robotic components. By combining the two, the proposed design offers a non-intrusive, non-toxic adaptable locomotive system that is can more easily be integrated with robotic systems for traversing challenging environments.

II. PROPOSED DESIGN & REQUIREMENTS

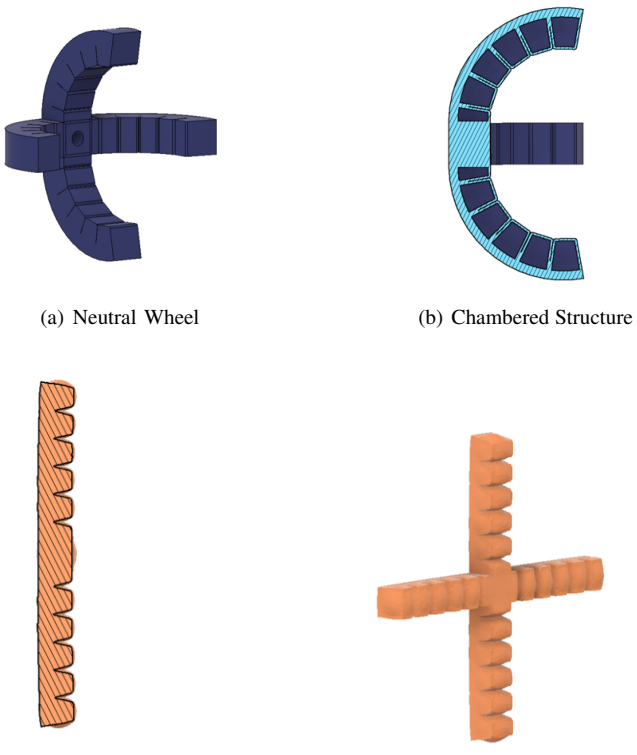

(a) Neutral Wheel

(b) Chambered Structure

(c) Inflated Structure

(d) Inflated Wheel

Fig. 1. Schematic for the proposed design

[1]Gaetan Pans is with Faculty of Mechanical Engineering, Delft, University of Technology, 2628CD Delft, The Netherlands gpans@tudelft.n l

[2] Dr. Jovana Jovanova with Faculty of Mechanical Engineering, University of Technology, 2628CD Delft, The Netherlands J.Jovanova@tudelft.nl

The proposed design (achieved after multiple design cycles, see Figure 1) is a completely soft wheel with 4 limbs where each limb is made up of inflatable hollow chambers as seen in 1(b). The individual limb design is based on common soft fluidic actuator which couples the inflatable hollow chambers with a strain-limiting layer on one side. When pressurised in a spatio-temporal manner, the stiffness differential causes deliberate and controlled deformation in one direction. Common shape configurations include pleated (also known as Pneunet), ribbed and cylindrical. As studied by Marchese et al., it was found that a pleated structure generates the highest tip force of the 3 configurations [3]. The wheel's controlled deformation adjusts its curvature and height, allowing a robot to adapt to rugged terrain. This enables the robot to climb over obstacles with extended limbs, pass under tight spaces by deflating them, and increase ground contact to prevent sinking in soft terrain.The neutral position is placed at maximum curvature such that at 0 pressure, the structure is still stable and cannot deform past the geometrical limit. The chambers are trapezoidal to make use of the stability of a triangular surface. This increases the surface area and therefore reduces the stresses throughout the structure.

With this, the requirements for the proposed design are as follows:

- Able to locomote over deformable terrain of varying moisture levels.
- Able to withstand a load of 1.25N (to operate on a 500g robot assuming 4 wheels).
- Non-destructive or intrusive to the surrounding environment
- Non-toxic to the surrounding environment

III. METHODOLOGY

A. Numerical and analytical model of soft wheel

For the simulation, a static structural analysis of the hyperelastic material used was run using FEM by commercial software. To improve computational efficiency, the model was simplified to a single limb (see Figure 2), focusing on the point of contact with the ground, which bears the highest loads. Simulating only a quarter of the design reduced the number of mesh elements and computation time.

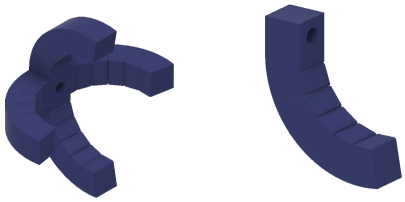

(a) Original Model (b) Simplified Model

Fig. 2. Geometric simplification

A large range of materials have been used for soft actuators, with silicone-based polymers being the primary choice due to their high maximum strain value [7] and being non-toxic to the surrounding environment. Hence, the elastomer with the highest shore hardness of the Dragon Skin series whilst maintaining a high strain failure rate [18] was selected.

Various strain energy functions (Ψ) can be used to characterise the hyperelastic model. For Dragon Skin 30, the 2nd-order incompressible Yeoh Model was most suitable to capture the stress-strain response, as it's suitable for large strain problems at or above 400% [5]. The experimental values obtained from Yang et al. for loading under uniaxial tension are $C_1 = 114.88$ kPa and $C_2 = 1.262$ kPa [17].

$$\Psi = C_1(I_1 - 3) + C_2(I_1 - 3)^2 \tag{1}$$

As for the simulation setup, a mesh size of 3mm was selected alongside linear order elements [5]. This facilitated convergence (using a coarse mesh size) whilst capturing the large deformation of each chamber as found by Tawk and Alici [4]. A frictional contact was set between all outer walls between the chambers with a coefficient of 0.2.

To verify the FEM model, an analytical model was developed. The analytical model is based on the principle of minimum potential energy (Γ) applied to an individual soft chamber. This can be defined as the sum of the internal material strain energy (U) and the work potential (W_p), This model builds on the approach proposed by Cao et al. [2]. As work is being done on the system (in this case pressure), it is assumed that the deformation caused is perfectly elliptical, resulting in an overall uniform curvature of the actuator as seen in Figure 3.

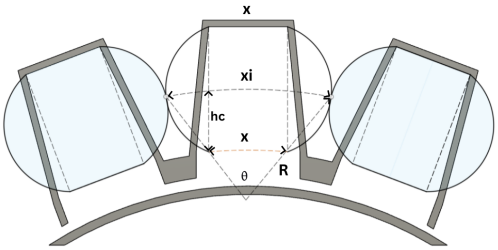

(a) Cross-Section View

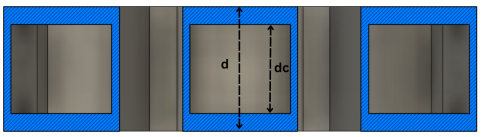

(b) Top View

Fig. 3. Schematic and geometry of the inflated chambers

From this, the following geometrical relationships can be made:

$$\theta = \frac{x_i}{R} = \frac{x}{R - h_c} \tag{2}$$

$$V_i = \frac{\pi}{4} h x_i d_c \tag{3}$$

Where the subscript i refers to the property when inflated. θ is the bending angle, R is the radius of curvature, x is the original chamber width, and x_i is the maximum inflated chamber width found at the centre of the ellipse. Additionally, h_c represents the distance to the centreline of the ellipse, h_1 is the distance from the base of a chamber to the top of the strain-limiting layer, and h is the total height of a chamber. Lastly, V_i denotes the inflated volume of a chamber.

(Γ) can be expressed as the internal strain energy of one chamber minus the work done due to the applied pressure to that chamber.

$$\Gamma = \frac{1}{2} D k_i^2 x_i - P_i V_i \tag{4}$$

$$D = EI \tag{5}$$

$$I = \frac{d h_1^3}{12} \tag{6}$$

where k is the curvature, D is the flexural rigidity, E is the elastic modulus, and I is the moment of inertia of the chamber. Additionally, P_i represents the inflation pressure.

However, due to the hyperelastic material properties, the elastic modulus cannot be constant and instead is a function of the strain. Using Equation yeoh hyperelastic model, the uniaxial stress-strain relationship can be obtained as follows, adopted from [5] where ϵ is the strain:

$$\sigma = 2\left((\epsilon+1)^2 - (\epsilon+1)^{-1}\right) \cdot \tag{7}$$

$$\left[C_1 + 2C_2\left((\epsilon+1)^2 + 2(\epsilon+1)^{-1} - 3\right)\right] \tag{8}$$

From Equation (7), the gradient can then be used as a function of strain to accommodate for the non-linearity. From here, Equation (4) and Equation (5) can be combined to get the following expression:

$$\Gamma = \frac{EIk_i^2 x}{1 - k_i h_c} - \frac{\pi P_i h x_i d_c}{4} \tag{9}$$

The point of equilibrium can then be found by solving $\frac{\partial \Gamma}{\partial k} = 0$. Solving for k and simplifying (taking the minimum of the quadratic solutions), the expression becomes:

$$k = \frac{EI - \sqrt{(EI)^2 - \frac{1}{2}\pi EI d_c h h_c^2 P_i \left(\frac{1}{2}\right)}}{EIh_c}. \tag{10}$$

From combining and simplifying Equation (2) and Equation (10):

$$\theta = \frac{x\left(EI - \sqrt{(EI)^2 - \frac{1}{2}\pi EI d_c h h_c^2 P_i}\right)}{h_c\sqrt{(EI)^2 - \frac{1}{2}\pi EI d_c h h_c^2 P_i}} \tag{11}$$

With the assumption that bending is uniform, the final expression for the bending curvature of the entire structure as a function of pressure is as follows, where N is the number of chambers:

$$N\theta = \frac{Nx\left(EI - \sqrt{(EI)^2 - \frac{1}{2}\pi EI d_c h h_c^2 P_i}\right)}{h_c\sqrt{(EI)^2 - \frac{1}{2}\pi EI d_c h h_c^2 P_i}} \tag{12}$$

This analytical model is used to verify the bending angle against pressure relationship from simulations before simulating the remaining loading configurations (LC). The bending angle in the simulation is determined by adding a probe on the end face that captures the average Eulerian angle between the starting position of the face and the end position.

Once verified, the design is simulated in 2 key loading configurations and the diagram of the loading configurations performed is shown in Figure 4. Firstly, a 0 pressure load test was conducted to ensure the design can support its self-weight even if not inflated. The self-weight as set by the requirements is a load of 1.25N. The second loading configuration is a blocked force test where the point of contact with the ground is fixed, and the pressure is ramped up from 0-50kPa. Through this, the maximum loading conditions of the design can be quantified to see the exerted force when changing the wheel's shape.

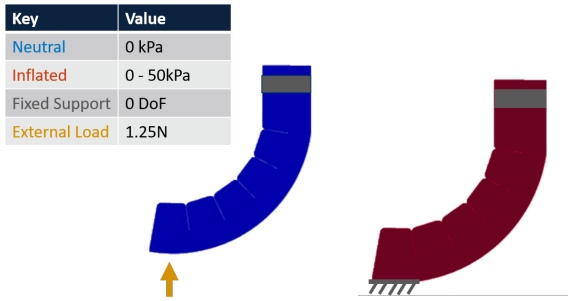

(a) 0 Pressure Load Test (b) Blocked Force Test

Fig. 4. Loading configurations performed to ensure structural feasibility

TABLE I
INPUT VALUES FOR ALL LC'S FOR THE FINAL DESIGN

LC	Applied Pressure (kPa)	Gravitational Acceleration (m/s^2)	Contact Force (N)
1	30	0	0
2	30	-9.81	0
3	0	-9.81	1.25
4	50	-9.81	NA

For the set of simulations, the maximum strain, maximum stress overall deformation profile are analysed to ensure no material failure as well as to understand operational characteristics. Material failure for Dragon Skin 30 occurs at a true stress value of 34MPa and strain of 700% [17].

B. Modelling of the deformable terrain and coupling

Once the model has been tested structurally, the DEM modelling coupled with multi-body dynamics was used to

test the resultant design in deformable terrain. As per the requirements set in section II, terrains of varying moisture and compressibility are tested to determine the versatility of the design. To model this, the built-in terrain material database from commercial software [19] was used, which includes the following four particle types: non-compressible dry, compressible dry, non-compressible sticky, and compressible sticky. The robot-particle interaction properties were sourced from tire and sandy soil studies [20]. The coefficient of restitution was varied linearly between 0.48 and 0.36 from non-compressible dry, non-compressible sticky, compressible dry and compressible sticky respectively. In addition, the Dragon Skin 30 is simplified to the standard rubber parameter for coupling. These specific material properties are shown in Table II.

TABLE II

ROBOT MATERIAL AND INTERACTION PROPERTIES

Parameter	Value
Sliding Friction (μ_s)	0.55
Rolling Friction (μ_r)	0.37
Density (ρ)	1100 kg/m^3
Poisson's Ratio (ν)	0.33
Elastic Modulus (E)	0.05 GPa

Due to the high computation required in generating a large number of particles, the terrain is limited to a size of 3 x 4 x 0.8m. In addition, 3 key operating configurations were chosen and exported in their deformed state, including neutral state, partially inflated state, and fully inflated state, shown in Figure 5.

(a) Neutral state (b) Partially inflated state (c) Fully inflated state

Fig. 5. Wheel operating configurations simulated in a deformable terrain

For each simulation, the terrain (30,000-35,000 particles) was filled and settled before coupling with the commercial software. The goal was to measure how far different wheel configurations traveled across various terrains in 5 seconds, with each joint set to a constant velocity of $2\pi rad/s$. MotionSolve then dropped the robot into the terrain and applied the forward velocity as seen in Figure 6. This process was repeated for each wheel configuration, running 12 simulations (4 sand types, 3 wheel configurations).

IV. RESULTS AND DISCUSSION

A. Numerical and analytical model of soft wheel

For verification of the model, it can be seen in Figure 7 that there is a strong agreement between the bending angle relationship derived from the 2 modelling methods. At

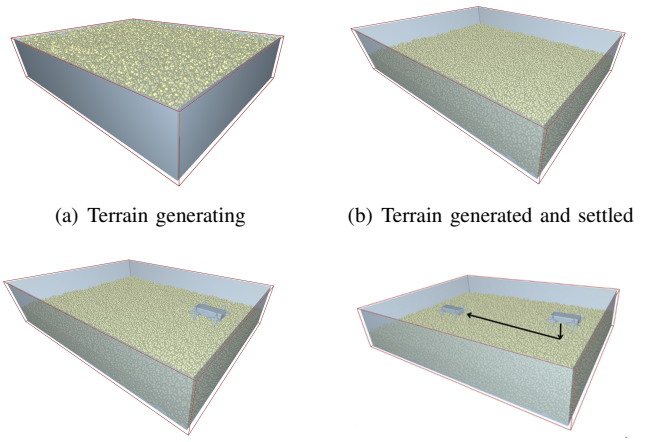

(a) Terrain generating (b) Terrain generated and settled

(c) Terrain coupled with multi-body dynamics of the robot (d) Path taken by robot during simulation

Fig. 6. Schematic for the simulation setup for deformable terrain testing

smaller input pressures (up to 15kPa), a deviation occurs due to the analytical model assuming uniform curvature across all chambers, while there is a delay between the initial pressurization in simulation and curvature throughout the structure. From Figure 8, it can be seen that at maximum bending angle, the strain distribution is uniform and no material failure occurs. With the system characterised (and the operational pressure being in the range of 0-30kPa under no-loading), the remaining loading configurations were simulated.

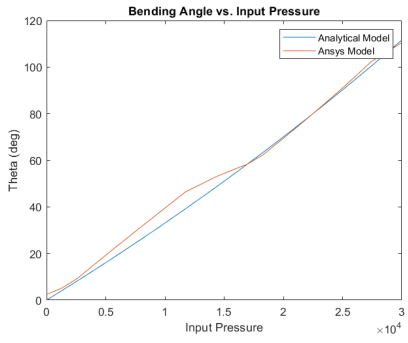

Fig. 7. Comparison of bending angle as a function of internal pressure for the final design. Modelled for LC1 comparing the analytical and numerical results

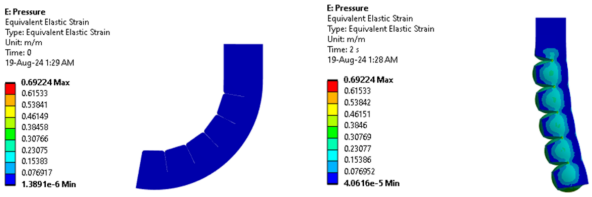

(a) Strain distribution at pre-LC1 (b) Strain distribution at post-LC1

Fig. 8. Uniform strain distribution before and after pressurisation for LC1

By comparing Figure 9(a) and Figure 9(b) it was seen that the final design proved stable at a 0kPa load test under 1.25N. The change in bending angle was negligible with the trapezoidal design acting as intended, to maintain the form of the wheel. This means that if needed a robot (of 500g assuming 4 wheels) could maintain operational even if no power was available for the shape change.

Regarding the blocked force test (Figure 10), it can be seen that at peak pressures of 50kPa it produced just upwards of 3N. However, when analysing the strain values at that point Figure (9(d)), although the system didn't experience material failure (see Table III) the distribution became significantly non-uniform and wouldn't provide stable operation. Hence, the operating blocked force was taken as 1.98N (at 35kPa) as that was the point where all chambers were still a uniform volume maintaining the curvature of the limb as seen in Figure 9(e).

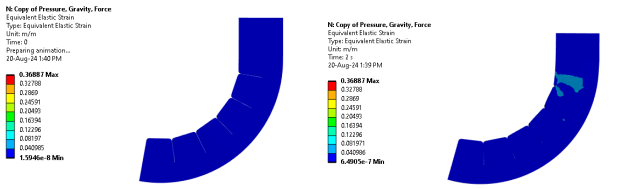

(a) Strain distribution at pre-LC3 (b) Strain distribution at post-LC3

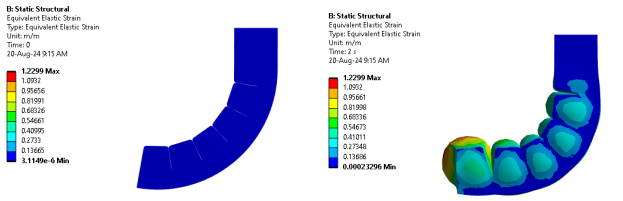

(c) Strain distribution at pre-LC4 (d) Strain distribution at post-LC4

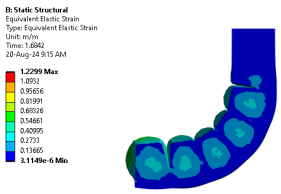

(e) Strain distribution at maximum operating point (LC4)

Fig. 9. Strain distribution for LC3 and LC4

TABLE III

LOAD CASES WITH MAXIMUM STRESS AND STRAIN VALUES FOR THE FINAL DESIGN

LC	Maximum Stress (kPa)	Maximum Strain (m/m)
1.1	449	0.69
1.2	451	0.69
1.3	848	0.37
1.4	878	1.23

The material and design feasibility was verified for its intended use using an analytical model and the finite element method. It can support its self-weight (500g as per the requirements set) whilst not undergoing material failure as seen in Table III.

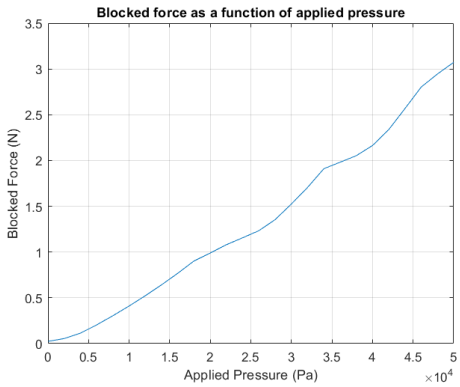

Fig. 10. Blocked force as a function of pressure until operational failure

B. Modelling of the deformable terrain and coupling

The results of concern are the distance travelled and the ride height. The first result, shown in Figure 11, is the robot's average height across all sand types. Height oscillation is caused by gaps between the wheel limbs, briefly lowering the robot. The amplitude and average height indicate how much the wheels sink into the terrain, with the neutral design sinking the least due to its larger contact area, despite its smaller diameter. The fully inflated design lifts the robot the most but sinks significantly with each rotation, while the partially inflated wheel sinks the deepest due to its curved surface.

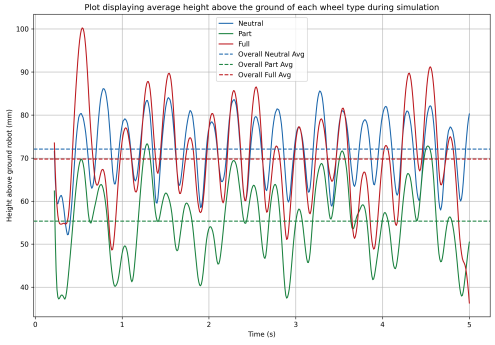

Fig. 11. Average height during simulation above the ground for each wheel configuration across all sand types

Figure 12 shows that the fully inflated design travels the farthest due to its larger diameter, though the neutral design's higher ride height allows it to travel the second farthest. Despite there being no terrain-dependent results in terms of distance covered, the height above the ground is terrain-dependent as seen in Figure 13. The neutral configuration performed best on compressible sticky and non-compressible dry terrains, while the fully inflated design excelled on less compressible surfaces.

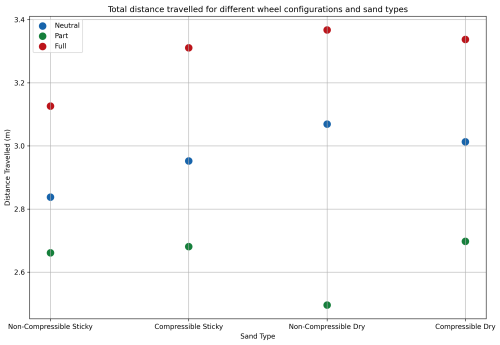

Fig. 12. Total distance travelled by each wheel configuration across all sand types

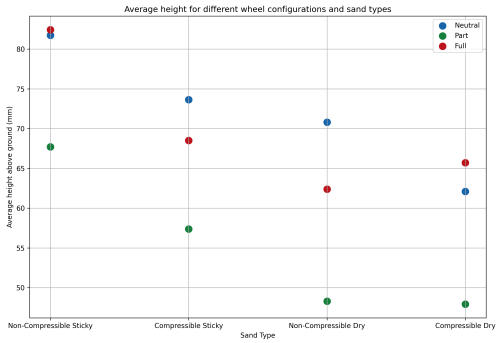

Fig. 13. Average height above the ground for each wheel configuration across all sand types

Overall, the adaptable system proves beneficial across varied terrains. Wheel geometry, contact area, and moisture levels all impact performance. The wheel is the least efficient when partially inflated, which can inform control strategies. Adaptability allows the robot to be multi-functional—if power efficiency is key, the neutral design is optimal as it requires no inflation and is stable across different terrains. For larger terrain variations or obstacles, the wheel geometry can be adjusted accordingly.

Its adaptable design lends itself to applications in more changing environments. Its intended terrain means potential use in agricultural settings, exploration, biodiversity monitoring and even potential space applications as the design can compress for transport and inflated 'on-site'.Its simplicity aids in creating other chassis designs beyond the simple 4-wheel option proposed in this project. A more detailed example would be a mangrove environment which is heavily rooted, constantly changing in moisture due to tides but crucial to ecosystems, erosion protection and economic stability of fishing villages. Hence the wheel can expand when needing to climb over roots and collapse when squeezing underneath them. Hence, it would be interesting to develop this idea further for amphibious terrains, with the wheel form having the potential to be utilised in a propeller setting. Examples of potential use cases can be seen in Figure 14. Future research efforts need to be taken to test the design, however, with the base locomotion (a rotation wheel) being simple, the hope is that it can more quickly be brought to application-based robotics due to its compatibility with off-the-shelf components.

V. CONCLUSION

It is challenging to increase the reach of robotic systems in environmental applications in a non-hazardous or damaging matter. The proposed solution has an operating pressure of 0-30kPa and was able to support a load of 1.25N in compression, making it suitable for a robot of 500g (given 4 wheels). It had an absolute maximum blocked force of 3N but an operational blocked for of 1.98N with non-uniform strain occurring over 35kPa. Finally, the model was tested in 4 different sand types at 3 different operating modes. The fully inflated wheel travelled the furthest due to its larger diameter, however did have larger oscillations and a lower overall ride height in comparison to the neutral wheel. The wheel when transitioning between states was the least efficient as it was the most submerged in the terrain.

This proposed design is aimed to be a starting point to increase the reach of robotic systems in environmental applications in a non-hazardous or damaging matter. Future work will involve manufacturing various prototypes to validate the concept and assess its lifespan in real-world settings, along with developing a control strategy for smooth robot operation and exploring individual limb actuation for greater compliance. The current design targets a 500g robot but can be scaled for different applications, with the potential for increased loading capabilities through composite materials or the use of particle jamming effects. Despite the challenge of needing both a DC motor and a compressor for actuation, the system remains stable at 0 kPa, prompting further research into lighter and more efficient batteries, motors, and pumps to enhance its performance in intended environments.

(a) A seed hopper for reforestation projects

(b) Biodiversity monitoring

(c) Lower ride height requirement for cave exploration

Fig. 14. Schematic for example use cases of the adaptive wheel concept

REFERENCES

[1] Shui, L., Zhu, L., Yang, Z., Liu, Y. & Chen, X. Energy efficiency of mobile soft robots. *Soft Matter*, **13**, 8223-8233 (2017).

[2] Cao, G., Chu, B. & Liu, Y. Analytical modeling and control of soft fast pneumatic networks actuators. In *Proceedings of the 46th Annual Conference of the IEEE Industrial Electronics Society (IECON)*, 2760-2765 (2020).

[3] Marchese, A., Katzschmann, R. & Rus, D. A recipe for soft fluidic elastomer robots. *Soft Robotics*. **2**, 7-25 (2015)

[4] Tawk, C. & Alici, G. Finite element modeling in the design process of 3D printed pneumatic soft actuators and sensors. *Robotics*. **9**, 52 (2020)

[5] Xavier, M., Fleming, A. & Yong, Y. Finite element modeling of soft fluidic actuators: Overview and recent developments. *Advanced Intelligent Systems*. **3**, 2000187 (2021)

[6] Smooth-On, I. Dragon Skin 30 Product Information. (2024), https://www.smooth-on.com/products/dragon-skin-30/, Accessed: 2024-07-29

[7] Trivedi, D., Rahn, C., Kier, W. & Walker, I. Soft robotics: Biological inspiration, state of the art, and future research. *Applied Bionics And Biomechanics*. **5**, 99-117 (2008)

[8] Ching, T., Lee, J., Win, S., Win, L., Sufiyan, D., Lim, C., Nagaraju, N., Toh, Y., Foong, S. & Hashimoto, M. Crawling, climbing, perching, and flying by FiBa soft robots. *Science Robotics*. **9**, eadk4533 (2024)

[9] Patel, A. Design and Analysis of Soft Actuator with Enhanced Stiffness with Granular Jamming. (University of Windsor (Canada),2022)

[10] El-Atab, N., Mishra, R., Al-Modaf, F., Joharji, L., Alsharif, A., Alamoudi, H., Diaz, M., Qaiser, N. & Hussain, M. Soft actuators for soft robotic applications: A review. *Advanced Intelligent Systems*. **2**, 2000128 (2020)

[11] Yap, Y., Sing, S. & Yeong, W. A review of 3D printing processes and materials for soft robotics. *Rapid Prototyping Journal*. **26**, 1345-1361 (2020)

[12] Shepherd, R., Ilievski, F., Choi, W., Morin, S., Stokes, A., Mazzeo, A., Chen, X., Wang, M. & Whitesides, G. Multigait soft robot. *Proceedings Of The National Academy Of Sciences*. **108**, 20400-20403 (2011)

[13] Tolley, M., Shepherd, R., Mosadegh, B., Galloway, K., Wehner, M., Karpelson, M., Wood, R. & Whitesides, G. A resilient, untethered soft robot. *Soft Robotics*. **1**, 213-223 (2014)

[14] Du Toit, V. Characterising material models for silicone-rubber using an inverse finite element model updating method. (Stellenbosch: Stellenbosch University,2018)

[15] Porte, E., Eristoff, S., Agrawala, A. & Kramer-Bottiglio, R. Characterization of temperature and humidity dependence in soft elastomer behavior. *Soft Robotics*. **11**, 118-130 (2024)

[16] Ghamsari, Z. The Introduction and Analysis of a Novel Soft Actuator for a Soft Continuum Robot Arm. (University of Minnesota,2018)

[17] Yang, F., Ruan, Q., Man, Y., Xie, Z., Yue, H., Li, B. & Liu, R. Design and optimize of a novel segmented soft pneumatic actuator. *IEEE Access*. **8** pp. 122304-122313 (2020)

[18] Agarwal, G., Besuchet, N., Audergon, B. & Paik, J. Stretchable materials for robust soft actuators towards assistive wearable devices. *Scientific Reports*. **6**, 34224 (2016)

[19] Altair Engineering Inc. (2022). *Soils Starter Pack*. Available at: `https://2022.help.altair.com/2022.2/EDEM/Creator/Soils_Starter_Pack.htm` [Accessed: August 11, 2024].

[20] Hu, C., Gao, J., Diao, J. & Song, X. Numerical simulation of tire steering on sandy soil based on discrete element method. *AIP Advances*. **11** (2021)

[21] Bai, X., Shang, J., Luo, Z., Jiang, T. & Yin, Q. Development of amphibious biomimetic robots. *Journal Of Zhejiang University-SCIENCE A 2022 23:3*. **23**, 157-187 (2022,3), https://link-springer-com.tudelft.idm.oclc.org/article/10.1631/jzus.A2100137

[22] Milana, E., Raemdonck, B., Cornelis, K., Dehaerne, E., Clerck, J., Groof, Y., Vil, T., Gorissen, B. & Reynaerts, D. EELWORM: A bioinspired multimodal amphibious soft robot. *2020 3rd IEEE International Conference On Soft Robotics, RoboSoft 2020*. (2020)

[23] Fracczak, Ł., Olejniczak, M. & Podsedkowski, L. Long-range snake-like robot powered by pneumatic McKibben muscles. *Archive Of Mechanical Engineering*. **66**, 257-267 (2019)

[24] Zhong, J., Luo, M., Liu, X., Fan, J. & Zhao, J. Frog-inspired jumping robot actuated by pneumatic muscle actuators. *Advances In Mechanical Engineering*. **10** (2018,6)

[25] Tolley, M., Shepherd, R., Mosadegh, B., Galloway, K., Wehner, M., Karpelson, M., Wood, R. & Whitesides, G. A Resilient, Untethered Soft Robot. *Soft Robotics*. **1**, 213-223 (2014,9)

[26] Kim, H., Song, S. & Ahn, S. A turtle-like swimming robot using a smart soft composite (SSC) structure. *Smart Materials And Structures*. **22** (2013)

[27] Klein, M., Boxerbaum, A., Quinn, R., Harkins, R. & Vaidyanathan, R. SeaDog: A rugged mobile robot for surf-zone applications. *Pro-*

ceedings Of The IEEE RAS And EMBS International Conference On Biomedical Robotics And Biomechatronics. (2012)

[28] Rus, D. & Tolley, M. Design, fabrication and control of soft robot using fluidic elastomer actuators. *Nature*. **521** (2015)